The Great Deceiver: miR-2392's Hidden Role in Driving SARS-CoV-2 Infection

J. Tyson McDonald[1,2], Francisco Javier Enguita[1,3], Deanne Taylor[1,4,5], Robert J. Griffin[1,6], Waldemar Priebe[1,7], Mark R. Emmett[1,8], Mohammad M. Sajadi[9], Anthony D. Harris[9], Jean Clement[9], Joseph M. Dybas[1,4], Nukhet Aykin-Burns[5], Joseph W. Guarnieri[1,4], Larry N. Singh[1,4], Peter Grabham[1,10], Stephen B. Baylin[1,11], Aliza Yousey[1,12], Andrea N. Pearson[12], Peter M. Corry[1,6], Amanda Saravia-Butler[1,13,14], Thomas R. Aunins[15], Sadhana Sharma[15,16], Prashant Nagpal[16,17,18], Cem Meydan[19], Jonathan Foox[19], Christopher Mozsary[19], Bianca Cerqueira[1,20,21], Viktorija Zaksas[1,22], Urminder Singh[1,23], Eve Syrkin Wurtele[1,23], Sylvain V. Costes[14], Gustavo Gastão Davanzo[24], Diego Galeano[1,25,26], Alberto Paccanaro[1,25,27], Suzanne L. Meinig[28], Robert S. Hagan[28], Natalie M Bowman[28], UNC COVID-19 Pathobiology Consortium[28+], Matthew C. Wolfgang[28], Selin Altinok[28], Nicolae Sapoval[29], Todd J. Treangen[29], Pedro M. Moraes-Vieira[1,24], Charles Vanderburg[30], Douglas C. Wallace[1,4,5], Jonathan Schisler[1,28], Christopher E. Mason[1,19,31], Anushree Chatterjee[1,15,16,17], Robert Meller[1,12], Afshin Beheshti[1,30,32,33,34*]

[1]COVID-19 International Research Team
[2]Georgetown University School of Medicine, Washington D.C. 20007, USA
[3]Universidade de Lisboa, Av. Prof. Egas Moniz, 1649-028 Lisbon, Portugal
[4]The Children's Hospital of Philadelphia, Philadelphia, PA 19104 USA
[5]University of Pennsylvania, Philadelphia, PA 19104 USA
[6]University of Arkansas for Medical Sciences, Little Rock, AK, 72211 USA
[7]University of Texas MD Anderson Cancer Center, Houston, TX, 77030, USA
[8]University of Texas Medical Branch, Galveston, TX 77555, USA
[9]University of Maryland School of Medicine, Baltimore, MD, 21201, USA
[10]Columbia University, New York, NY 10032, USA
[12]Johns Hopkins School of Medicine, Baltimore, MD 21287, USA
[12]Morehouse School of Medicine, Atlanta, GA 30310, USA
[13]Logyx, LLC, Mountain View, CA 94043, USA
[14]NASA Ames Research Center, Moffett Field, CA 94035, USA
[15]University of Colorado Boulder, Boulder, CO, 80303, USA
[16]Sachi Bioworks Inc, Boulder, CO, 80301, USA
[17]Antimicrobial Regeneration Consortium, Boulder Labs, CO, 80301, USA
[18]Quantum Biology Inc, Boulder, CO, 80301, USA
[19]Weill Cornell Medicine, NY, 10065, USA
[20]KBR Space & Science, San Antonio, TX, 78235, USA
[21]United States Air Force School of Aerospace Medicine, Lackland AFB, TX, 78236, USA
[22]University of Chicago, Chicago, IL, 60615, USA
[23]Iowa State University, Ames, IA 50011, USA
[24]University of Campinas, SP, Brazil
[25]Fundação Getulio Vargas, Rio de Janeiro, Brazil
[26]National University of Asuncion, Central, Paraguay
[27]University of London, Egham Hill, Egham, UK
[28]University of North Carolina at Chapel Hill, Chapel Hill, NC, 27599, USA
[29]Rice University, Houston, TX 77005, USA

[30]Broad Institute of MIT and Harvard, Cambridge, MA, 02142, USA
[31]New York Genome Center, NY, USA
[32]KBR, NASA Ames Research Center, Moffett Field, CA, 94035, USA
[33]Senior author
[34]Lead Contact
+The full list of authors associated with the UNC COVID-19 Pathobiology Consortium is available in the supplemental information.
*Correspondence: afshin.beheshti@nasa.gov

Summary

MicroRNAs (miRNAs) are small non-coding RNAs involved in post-transcriptional gene regulation that have a major impact on many diseases and provides an exciting avenue towards antiviral therapeutics. From patient transcriptomic data, we have discovered a circulating miRNA, miR-2392, that is directly involved with SARS-CoV-2 machinery during host infection. Specifically, we show that miR-2392 is key in driving downstream suppression of mitochondrial gene expression, increasing inflammation, glycolysis, and hypoxia as well as promoting many symptoms associated with COVID-19 infection. We demonstrate miR-2392 is present in the blood and urine of COVID-19 positive patients, but not detected in COVID-19 negative patients. These findings indicate the potential for developing a novel, minimally invasive, COVID-19 detection method. Lastly, using *in vitro* human and *in vivo* hamster models, we have developed a novel miRNA-based antiviral therapeutic that targets miR-2392, significantly reduces SARS-CoV-2 viability in hamsters and may potentially inhibit a COVID-19 disease state in humans.

Key words

COVID-19, SARS-CoV-2, microRNA, miRNA, Nanoligomers, miR-2392, antiviral therapeutic

Introduction

In Fall of 2019, the zoonotic spillover event led to the first known human infection with the severe acute respiratory syndrome coronavirus 2 (SARS-CoV-2) and subsequent human-to-human transmission triggered a pandemic leading to a worldwide health crisis from the resulting disease, referred to as coronavirus disease 2019 (COVID-19) (Huang et al., 2020; Zhu et al., 2020). COVID-19 causes substantial pulmonary disease but can also cause systemic health risks from extrapulmonary manifestations. Its effects entangle the entire body including but not limited to the cardiovascular, gastrointestinal, and hematological systems that may lead to long lasting effects after the virus has left the body, known as PASC (post-acute sequela of COVID-19) (Carfi et al., 2020; Feng et al., 2020; Jacobs et al., 2020). SARS-CoV-2 is classified as a member of the Coronaviridae family, viruses with a enveloped positive-stranded RNA with the ability to infect cross-species (V'Kovski et al., 2021). Currently, three vaccines have been approved for emergency use by the Food and Drug Administration (Baden et al., 2021; Polack et al., 2020; Sadoff et al., 2021). While these vaccines represent a favorable milestone, additional data is required to demonstrate their long-term effectiveness against SARS-CoV-2 and protection against new strains. To prevent an endemic, the complete global eradication of COVID-19 will require a wide majority of the world's population to be vaccinated to achieve herd immunity. Unfortunately, a portion of the population will not get vaccinated. Therefore, strategies for therapeutic options

against COVID-19 are particularly relevant and important to explore to treat severe illnesses and overcome this global pandemic. Currently the majority of antivirals are repurposed drugs utilized for other disease and have shown limited clinical efficacy, such as remdesivir (Abdelrahman et al., 2021). This brings a needed urgency to develop antivirals specifically designed against SARS-CoV-2.

A potential avenue for an alternative antiviral agent is to target specific microRNAs (miRNAs) associated with SARS-CoV-2 infection and subsequent manifestation of COVID-19. MicroRNAs (miRNAs) are non-coding RNAs that are involved with regulation of post-transcriptional gene expression and can impact entire pathways related to viruses and diseases (Jiang et al., 2009; Trobaugh and Klimstra, 2017). Each miRNA can target multiple messenger RNAs (mRNAs) and taken together, miRNAs are predicted to regulate over half of the human transcriptome (Friedman et al., 2009). Recent evidence has shown different diseases, including COVID-19, leads to distinct complements of miRNAs in the blood (Mishra et al., 2020; Nersisyan et al., 2020; Sacar Demirci and Adan, 2020; Teodori et al., 2020). These circulating miRNAs are highly stable and have the potential to be used for minimally invasive novel detection, potential biomarkers, and therapeutic targets (Tribolet et al., 2020). The interactions between miRNAs and viruses have revealed a multifaceted relationship. Specifically, viruses have been shown to avoid the immune response by leveraging cellular miRNAs to complete their replication cycle (Trobaugh and Klimstra, 2017). The following mechanisms are central to the interaction of viruses and miRNAs: 1) miRNA processing can be blocked by viruses interacting with key proteins such as Dicer and associated proteins, 2) viruses can sequester miRNAs resulting in dysregulation of specific target mRNAs, 3) viruses can utilize miRNAs to redirect regulatory pathways of other miRNA targets to provide survival advantages, and 4) viruses can directly encode miRNA precursors that are processed by the canonical miRNA cellular pathway and have well-defined functions to specifically target and regulate the viral replicative cycle (Schult et al., 2018; Trobaugh and Klimstra, 2017).

Here, we report on a miRNA, miR-2392, that may directly regulate and drive a COVID-19 response. This miRNA is predicted from COVID-19 RNA-sequencing patient data that resulted in multiple miRNAs being suppressed/inhibited (miR-10, miR-10a-5p, miR-1-3p, miR-34a-5, miR-30c-5p, miR-29b-3p, miR-155-5p, and miR-124-3p) and one miRNA being upregulated (miR-2392). With further examination, we hypothesize miR-2392 to be a key miRNA involved with COVID-19 progression. Specifically, miR-2392 drives downstream suppression of mitochondria activity while increasing inflammation, glycolysis, and hypoxia. MiR-2392 upregulation is concomitant with symptoms associated with COVID-19 infection in the host. Patient blood and urine data show that miR-2392 circulates in COVID-19 infected patients and its concentration increases as a function of viral load. Our results demonstrate that miR-2392 may be utilized as an effective biomarker of COVID-19. Furthermore, we have started development of a miR-2392 inhibitor and provide evidence that its use reduces SARS-COV-2 viability in targeted viral screens with A549 cells and reduces the impact of infection in COVID-19 animal models. With further development this miR-2392 inhibitor may represent an effective antiviral therapeutic towards inhibiting the virus and limiting a negative host response from COVID-19 in humans.

Results

Identification of key miRNAs associated with COVID-19 infection

Currently, the majority of publications associated with miRNAs and SARS-CoV-2 are based on *in silico* predictions. To identify miRNAs that may be involved in driving COVID-19 severity in the host, we examined publicly available Bronchial Alveolar Lavage Fluid (BALF) RNA-sequencing (RNA-seq) data from 13 individuals. Differential gene expression was assessed using a 1.2-fold changes for p-values less than 0.01 revealing 42 increased and 347 decreased genes compared to controls. Using the upstream regulator analysis from the Ingenuity Pathway Analysis (IPA) knowledge database, the miRNAs from differentially expressed genes (FDR<0.05) from COVID-19-positive patients were inferred. Eight miRNAs were predicted to drive significant changes in COVID-19 positive patients with the downregulation of seven miRNAs (miR-10, miR-1, miR-34a-5p, miR-30c-5p, miR-29b-3p, miR-124-3p, and miR-155-5p) and upregulation of a single miRNA, miR-2392 (**Fig. 1A**). Using IPA's downstream effects analysis to predict biological processes from the combined suppression of the seven miRNAs and the upregulation of miR-2392 resulted in increased inflammation, immune suppression, and suppression of mitochondrial activity in the BALF dataset (**Fig. 1B and 1C**).

In support of these findings, previous studies have shown upregulation of miR-10, miR-124, or miR-1 have antiviral roles during infection (Hu et al., 2020; Sardar et al., 2020; Yang et al., 2016) and upregulation of miR-30 and miR-155 causes suppression of other coronaviruses (Dickey et al., 2016; Ma et al., 2018). The one miRNA predicted to be upregulated in COVID-19 patients from the BALF data was miR-2392. Though limited, the existing literature on miR-2392 demonstrates it is related to mitochondrial suppression and increased glycolysis (Fan et al., 2019) and circulating factors related to negative health risks (Chen et al., 2013; Fan et al., 2019; Li et al., 2017; Yang et al., 2019).

We performed pathway analysis with miR-2392 targets to determine its potential impact on the host. Upregulation of miR-2392 in the BALF RNA-seq dataset impacted many downstream targets and pathways related to negative health outcomes (**Fig. 1C**). This includes mitochondrial suppression and activation of factors related to reactive oxygen species (ROS). Since it is known that miR-2392 directly interacts with mitochondrial DNA (mtDNA) to inhibit the levels of oxidative phosphorylation transcripts (Fan et al., 2019), this could be a compensatory response to the inhibition of mitochondrial bioenergetics.

Glycolytic pathways (**Fig. 1C**) are also upregulated in association with increased miR-2392. MiR-2392 drives both hexokinase 2 (HK2) and pyruvate kinase (PKM), both of which positively regulate glycolysis. HK2 produces a primary regulator of glycolysis, glucose-6-phosphate and enhances GDP-glucose biosynthesis. GDP-glucose is a nucleotide sugar which an essential substrate for all glycosylation reactions (i.e. glycosylation of viral spike proteins). PKM is essential for the production of ATP in glycolysis that catalyzes the transfer of the phosphate group from phosphoenolpyruvate to ADP to make ATP. The mechanism of how miR-2392 is driving these pathways is not clearly understood, but one possibility could be stabilization of glycolytic transcripts.

Overall, the observed upregulation of glycolysis and antiviral effects related to miR-2392 suppression are consistent with the recently documented role of glucose metabolism in the progression of viral infection and poor outcome of COVID-19 (Ardestani and Azizi, 2021). It is also consistent with the reported effects of suppression of glycolysis by inhibitors like the glucose

analog, 2-deoxy-D-glucose (2-DG), that was shown to suppress *in vitro* SARS-CoV-2 replication (Ardestani and Azizi, 2021; Bojkova et al., 2020). Interestingly, 2-DG is also 2-deoxy-D-mannose and as such can interfere with processes utilizing mannose, a monosaccharide that is produced *in vivo* from glucose. Replacement of a mannose molecule by 2-DG in the respective SARS-CoV-2 N- or O-glycans might lead to their truncation and suppression of virus infectivity and proliferation. These and miR-2392 data indicate targeting of glucose metabolism might have significant impact on SARS-CoV-2 infections.

Targets implicated in antioxidant N-acetyl cysteine (NAC) therapy are to be upregulated (**Fig. 1C**). These include adhesion molecules of activated endothelial cells such as intercellular adhesion molecule 1 (ICAM1), vascular cell adhesion molecule 1 (VCAM1), and E-selectin, which allow attachment of hematopoietic immune and non-immune cells to the endothelial surface, and thus, contribute to inflammation and activation of the coagulation cascade. Powerful antioxidants such as NAC potentially counteract COVID-19 infections by suppressing viral replication via improving intracellular thiol redox ratio as a precursor for major thiol antioxidant glutathione (Ho and Douglas, 1992) and inhibiting the NF-kB pathway (Poppe et al., 2017). Inhibition of the NF-κB pathway reduces inflammatory damage by altering the glutathione and glutathione disulfide ratio (Aykin-Burns et al., 2005; Griffin et al., 2003; Jia et al., 2010). Because NAC can also modulate oxidative burst and reduce cytokine storm without weakening the phagocytizing function of neutrophils (Aykin-Burns et al., 2005; Jia et al., 2010), clinical trials in COVID-19 patients are being conducted (Alamdari et al., 2020) to reduce severe infection (Ibrahim et al., 2020). These results were in line with the role of miR-2392 in reducing the activities of electron transport chain complexes and enhancing glycolysis. It is also speculated that NAC could inhibit binding to ACE2 by reducing disulfide bonds in the receptor-binding domain. Inflammatory pathways and others that are observed with COVID-19 infection were also seen to be activated downstream of miR-2392.

Conservation of miR-2392 between species and its predicted interactions with the SARS-CoV-2 genome

Viral miRNAs can facilitate interspecies viral transmission due to the high conservation of miRNAs among species and the ability of viruses to integrate miRNAs into its own genome (Sacar Demirci and Adan, 2020; Schult et al., 2018). This has been shown to assist viral replication and evasion of the immune system (Islam and Islam, 2021). Thus, we analyzed the conservation of human miR-2392 across species and the integration of miR-2392 into the SARS-CoV-2 genome (**Fig. 2**).

We determined the conservation of miR-2392 across different species using the UCSC Genome Browser (Kent et al., 2002). The mature 20 base-pair miR-2392 is derived from an 84 base-pair region of the 3´-UTR in the long non-coding RNA gene, maternally expressed 3 (MEG3) and is located in an imprinted region DLK1-DIO3 that contains three clusters with 51 other miRNAs (**Fig. 2A and 2B**). A basewise evolutionary comparison showed miR-2392 is highly conserved among non-human primates such as dogs, cats, and ferrets, species known to be infected with SARS-CoV-2 while mice and rats, species not impacted by COVID-19 (Johansen et al., 2020), have poor conservation with miR-2392.

The impact of miR-2392's host gene, MEG3, within normal tissues was determined utilizing GTEx data (Consortium, 2020). For the majority of healthy tissues, MEG3 was either not detected or being expressed at low levels (**Fig. 2B**). This can imply that miR-2392 does not seem to significantly affect normal tissues.

We used miRanda (Enright et al., 2003) to identify potential miR-2392 binding sites with respect to the SARS-CoV-2 reference genome (Wuhan-Hu-1; NC045512.2) and lineages of concern. The miR-2392 seeding region is heavily integrated and conserved in different viral strains (**Fig. 2C**). The three best scores are located in the NSP2, NSP3, and E-genes. Notably, these regions were conserved among 6 concerning lineages represented by 14 recent genomes available from the Global Initiative on Sharing All Influenza Data (GISAID, (Shu and McCauley, 2017)).

MiR-2392 targets mitochondrial and inflammatory pathways associated with SARS-CoV-2

To determine a more comprehensive impact of miR-2392 affected pathways in COVID-19 patients, gene targets were predicted by seed-region base pairing in the miRmap database (Vejnar and Zdobnov, 2012). This list was refined by overlap in several miRNA databases including miRmap, miRwalk (Dweep and Gretz, 2015), miRDB (Chen and Wang, 2020), miRnet (Chang et al., 2020), and ClueGo (Bindea et al., 2009). We added RNA-seq analysis of 39 autopsy tissue samples from the heart, lung, kidney, liver, and lymph node of COVID-19-positive patients with high or low viral loads (Park et al., 2021). MiR-2392 gene targets (375 genes) were visualized using volcano plots (**Fig. 3A-F**).

To further ascertain the systemic impact on miR-2392 gene targets in COVID-19, we performed pathway analysis from the nasopharyngeal swab samples taken from living donors with and without COVID-19 using the SARS-CoV-2 viral load as the independent variable (high, medium, low, other virus). The differentially expressed genes (FDR<0.05) in at least one comparison of COVID-19-positive patients or other detected virus and were found to separate into six distinct hierarchical clusters that were annotated using ShinyGO (Ge et al., 2020) (**Fig. 3G**). The majority of the upregulated miR-2392 targets participate in immune and inflammatory pathways. Downregulated targets are involved in mitochondrial function, oxidative stress, cell cycle, developmental biology, and ubiquitin binding, all pathways recently associated with SARS-CoV-2 infection (Hemmat et al., 2021). This data demonstrates miR-2392 may target several pathways related to perpetuating SARS-CoV-2 infection. For all tissues excluding the lymph nodes, higher viral loads are associated with greater differential expression of miR-2392 regulated gene targets.

Since miR-2392 was recently shown to directly target the transcription of mitochondrial DNA genes (Fan et al., 2019), we evaluated mitochondrial miR-2392 targets in our datasets using MitoCarta (Rath et al., 2021) (**Fig. 3H**). This revealed 14 genes harboring miR-2392 seed sequences that were significantly dysregulated in the nasal and heart samples. In nasal samples, SLC25A28, a mitoferrin which mediates mitochondrial iron transport, was strongly upregulated along with IBA57, which is involved in iron sulfur assembly. The mitochondrial outer membrane protein import complex subunit TOMM20, cytochrome c oxidase (complex IV) subunit COX6B1, and mitochondrial transcription factor COT-2 (NR2F2) were strongly downregulated. In the heart, the folate enzyme MTHFD2L (methylenetetrahydrofolate dehydrogenase) was upregulated while all of the other nuclear-coded mitochondrial genes were downregulated. Downregulated heart

mitochondrial genes included NDUFS5 (complex I subunit), COX6B1 and COX10 (complex IV structural and assembly subunits), CKMT1A (mitochondrial creatine kinase), MRPL34 (mitochondrial ribosome small subunit), COT-2 (NR2F2), AK4 and MSRB3 (adenylate kinase 4 and methionine-R-sulfoxide reductase which mitigate oxidative stress), MRS2 (magnesium transporter) and CLIC4 (chloride channel). The kidney showed mild upregulation of complex I and single methyl group metabolism, but down regulation of complex IV (COX10), regulatory factor (COT-2), and iron sulfur center protein (IBA57). Hence, SARS-CoV-2 seems to downregulate nuclear mitochondrial gene transcription in the more oxidative organs, heart and kidney, as well as in nasal tissues.

Since inflammation is a key component of COVID-19, we overlaid known inflammatory genes determined from Loza et al. (Loza et al., 2007) with miR-2392 targets (**Fig. 3I**). From analysis at the mRNA level, most of the complement pathway genes are upregulated in the tissue samples analyzed. These changes could be compensatory, as proteins encoded by the genes could be downregulated as a function of traditional miRNA effects. The responses reflect the importance of degrees of inflammation for mediation of disease severity in COVID-19 patients and a key modulatory role of miR-2392 in this context.

Proteomic and transcriptomic analysis in blood from COVID-19 patients utilizing COVIDome (Sullivan et al., 2021) revealed interesting patterns between RNA and protein levels for miR-2392 targets from miRmap, ClueGO, miRwalk, miRnet, and miRDB (**Fig. 3J and 3K**). Several miR-2392 targets in tissue show a significant transcriptional increase in COVID-19-positive samples with small to no changes on the proteomics level: PLK1, CD38, PYCR1, RNASE1, BIRC5, RRM2, SIGLEC1 (**Fig. 3J**). Interestingly, all these genes were also positively regulated for the majority of tissues when considering only miR-2392 gene targets with miRmap (**Figs. S1 and S2**). The miR-2392 targets CXCL10, STAT1, IFIT3, and C1QC were positively regulated at both the protein and gene levels for the blood and other tissues. The correlation between RNA and protein expression was very close for miR-2392 targets and was slightly stronger in COVID-19 negative (cor=0.209, p=4e-10) versus positive (cor=0.205, p=8e-10) samples (**Fig. 3K**). Further investigation is needed to understand if increased levels of miR-2392 could potentially bind genes' mRNAs at a higher rate and therefore prevent translation to protein or if there are other mechanisms preventing mRNA translation to protein.

Overexpression of miR-2392 simulates a phenotype similar to COVID-19 infection

To determine if miR-2392 upregulation would elicit effects similar to a COVID-19 infection, cells were treated with a miR-2392 mimic. Using RNA-seq, 649 genes had a fold-change greater than ±1.2 and a p-value less than 0.05 (**Fig. 4A**) and many genes were miR-2392 predicted targets (**Fig. 4B**). These genes were then compared to whole cell proteome data from a human-derived cell culture model of a SARS-CoV-2 infection profile (Stukalov et al., 2021) and found 10 overlapping gene/proteins that were significantly altered: KIF22, FKBP14, RAD51, AFAP1, ZCCHC17, ZWINT, MAGED1, CENPF, TMEM70, and NFKB2 (**Fig. 4C**). Because viral infection may alter post-translational modification including ubiquitination, we analyzed the ubiquitinome of a SARS-CoV-2 human-derived cell culture model and observed a number of altered proteins in normalized ubiquitin abundance that were also dysregulated genes by miR-2392

overexpression. We also found miR-2392 overexpression impacted genes involved with mitochondria and inflammation (**Fig. 4D-4F**).

To determine if there was a direct correlation between miR-2392 overexpression and SARS-CoV-2 infection, we compared gene expression changes or overlap in statically significant canonical gene sets with our fGSEA analysis. Published data from Blanco-Melo *et al.* (Blanco-Melo et al., 2020), showed a statistically significant and positive correlation of the miR-2392 treatment to the A549 and Calu-3 cells infected with SARS-CoV-2 (**Fig. 4G and 4H**) as well as in lung biopsies post-mortem from two COVID-19 positive patients (**Fig. 4H**). Using nasal swab samples, there was a significant and positive correlation between patients with medium- and low-viral loads compared to non-infected patients (**Fig. 4I and 4J**). Additional miR-2392 correlation to SARS-CoV-2 infections used RNA-seq data from multiple tissues (heart, kidney, liver, lymph node, and lung) obtained during autopsies of COVID-19 patients with high or low viral loads (**Fig. 4I-J**). There was a positive correlation to lung and lymph node tissues with miR-2392 expression. Interestingly, there was a significant and positive correlation to liver tissue when comparing gene fold-change values (**Fig. 4I**) but not C2 curated biological genesets (**Fig. 4J**). In contrast, a negative correlation to heart tissue was observed.

Statistically significant pathways that were enriched due to miR-2392 treatment were examined using fGSEA **(Fig. 4K-O)**. MiR-2392 treatment induced a pathway response that was significantly related to SARS-CoV-2 pathways. One obvious relationship shows that the Reactome SARS-CoV-2 pathways were significantly activated for the miR-2392 treated cells compared to the controls (**Fig. 4K and 4L**). Significant Hallmark pathways (**Fig. 4N**) show upregulation of hypoxia (Herrmann et al., 2020), glycolysis (Ardestani and Azizi, 2021), and cell cycle pathways (Su et al., 2020) that have been reported to be associated with COVID-19. Interestingly, the KEGG pathway analysis (**Fig. 4M**) indicates miR-2392 overexpression highly upregulated systemic lupus erythematosus which has been reported to occur in COVID-19 patients and have shown similar pathologies due to the increase of inflammation (Zamani et al., 2021).

Lastly, we determined downregulated targets in the cell lines after miR-2392 overexpression. A regulatory network was built by including the predicted miR-2392 targets in the microRNA Data Integration Portal (MIRDIP) that were also downregulated in the overexpression cell model as well as from the recently described consensus transcriptional regulatory networks in coronavirus infected cells (Ochsner et al., 2020) (**Fig. 4P**). The gene enrichment analysis of these putative miR-2392 targets showed the presence of GO-terms related with the RNA metabolism, transcription, ribosome activity and Golgi complex (**Fig. 4Q**).

Circulating miR-2392 and the suppression of other miRNAs in COVID-19 infected patients

To demonstrate the presence of circulating miR-2392 in COVID-19 infected patients, we quantified the amount of miR-2392 by droplet digital PCR (ddPCR) in the serum, urine and nasopharyngeal swab samples (**Fig. 5**). Serum was obtained from 20 COVID-19 positive patients (10 intubated, 10 not intubated) and ten negative patients. Urine samples were collected from 30 COVID-19 positive patients (15 inpatient, 15 outpatient), 10 inpatient COVID-19 negative samples, and 11 COVID-19 negative healthy donors. Nasal swab samples were obtained from 10 COVID-19 positive patients, 6 common cold coronavirus positive patients (229E, HKU1, and OC43), and 6 Respiratory Illness/Coronavirus NL63 positive patients.

We observed a statistically significant increase of miR-2392 in COVID-19 positive patients from both the serum and urine samples (**Fig. 5A**). In addition, Receiver Operating Characteristic (ROC) curve analysis revealed that miR-2392 is significantly associated with SARS-CoV-2 infection in patients (**Fig. 5B**) in all tissues. MiR-2392 levels were higher for conditions associated with infection of more severely affected patients (i.e. intubated or ICU) (**Fig. 5C**). Interestingly, low levels miR-2392 appeared in the nasopharyngeal location with no significant differences occurring between seasonal coronavirus samples. To study more specific tissue origins for miR-2392 we infected monocytes obtained from healthy donors with SARS-CoV-2 reference strain (i.e. strain from Wuhan) and also P1 variant (**Fig. 5D**). We saw an increase of miR-2392 with the reference SARS-CoV-2 infected cells and a significant increase in the P1 variant infected cells. Previously, it was shown that these monocytes infected with SARS-CoV-2 have increased pro-inflammatory cytokine and glycolysis expression, with the effects inhibited by glycolysis inhibitors (Codo et al., 2020). Since we hypothesize that miR-2392 is a primary initiator for systemic impact of the infection, this might indicate that miR-2392 does not strongly appear until the virus has established its presence in the body.

We also quantified miR-1-3p (**Fig. S3**), miR-155-5p (**Fig. S4**), and miR-124-3p (**Fig. S5**) which were predicted to be inhibited by COVID-19 infection (**Fig. 1A**). MiR-1-3p and miR-155-5p were significantly suppressed in the serum with no differences in the urine or nasopharyngeal samples (**Fig. S3 and S4**). MiR-1-3p is known to be beneficial for cardiovascular functions, with its inhibition leading to heart failure and disease (Condorelli et al., 2010). Interestingly, when quantifying miR-1-3p in the SARS-CoV-2 infected monocytes we observe a significant decrease with the reference strain, while no different with the P1 variant (**Fig. S3D**). For miR-124-3p, we observed very low amounts (on average < 2 copies/5 ng RNA), for all conditions, which indicates that miR-124-3p is not circulating for any of the patients for any the conditions observed (**Fig. S5**). MiR-124-3p provides an ideal miRNA negative control candidate for SARS-COV-2.

Inhibiting miR-2392: a novel antiviral COVID-19 therapeutic

The link between miR-2392 and COVID-19 infection prompted the develop of an effective antiviral approach for COVID-19 by inhibiting miR-2392. We used the Nanoligomer platform to develop an effective antisense-based therapeutic against human miR-2392 (Eller et al., 2021), termed SBCov207 (**Fig. 6A**). The anti-miR-2392 Nanoligomers was evaluated for efficacy and toxicity against a SARS-CoV-2 infection of the human lung cell line A549 (**Fig. 6B-D**). Treatment of uninfected A549 cells showed no cytotoxicity up to 20 µM. The control nonsense Nanoligomers (SBCoV208) showed no toxicity even up to 40 µM. Treatment of A549 cells infected with SARS-CoV2 showed drastic improvement in cell viability with an average of 85% viral inhibition at 10 µM (IC50=1.15±0.33 µM). In contrast, the control Nanoligomers showed significantly lower viral suppression (**Fig. 6E-G**). This human cell line model reaffirms that the anti-miR-2392 (SBCov207) is effective in inhibiting SARS-CoV2, while not exhibiting toxicity at the concentrations tested.

The anti-miR-2392 Nanoligomers was then evaluated in a Syrian hamster infection model (**Fig. 6H-6J**). Six hamsters were treated with Nanoligomers for 72 hours without infection and there was no observed change in animal behavior indicating a lack of obvious toxicity. Next, 30 male hamsters were divided into 5 treatment groups. The infected hamsters were given 10^5 plaque

forming units (pfu) of WA01/2020 strain of SARS-CoV-2. The anti-miR-2392 Nanoligomers treatment was given by intraperitoneal (IP) injection or intranasal (IN) instillation once at 24 hours before or twice at 24 hours before and after viral inoculation. Half of the hamsters in each group (n=3) were euthanized and necropsied on day 3 and 7 post-infection respectively.

Loss of body weight over the course of the experiment was <10% in all groups and significantly different for the IN treatment one day before viral inoculation (compared to the control) while statistical differences in other groups were not present (**Fig. 6H**). Virus titers from oropharyngeal swabs for IN treatment were significantly lower (p = 0.018) than those from hamsters receiving Nanoligomers IP or PBS on day 1 post-challenge, but there were no differences among groups on days 2 and 3 post-challenge (**Fig. 6I**). Although not statistically different than the control treatment, the data indicates a downward trend with Nanoligomers treatment (**Fig. 6J**) and the total histopathological score for the IN was lower than the controls.

The impact of miR-2392 on diseases, relationship to COVID-19 symptoms, and predicted FDA drugs to target miR-2392

To predict whether miR-2392 might have a direct relationship to COVID-19 symptoms, we determined the pathway and disease relevance using miRnet. Among the diseases predicted to be associated with miR-2392 were a surprising number of clinical observations present in individuals with COVID-19 infection (**Fig. 7A**). These include heart or cardiovascular disease and failure, both known to heavily contribute to morbidity and mortality in patients with COVID-19 (Nishiga et al., 2020), hyperesthesia (Krajewski et al., 2021), as well as less common COVID-19 symptoms, such as lymphadenopathy and pharyngitis related to sore throat (Edmonds et al., 2021), liver dysfunction (Portincasa et al., 2020), splenomegaly (Malik et al., 2020), CNS (Mahajan and Mason, 2021; Rodriguez et al., 2020) and kidney failure (Hultstrom et al., 2021).

MiR-2392 was also predicted to affect other diseases that have been linked to COVID-19 infection in some patients. For example, COVID-19 patients have experienced azoospermia, which is linked to male infertility (Younis et al., 2020), altered menstrual cycle in females (Li et al., 2021), dental damage (Sirin and Ozcelik, 2021), and deafness or hearing loss (Koumpa et al., 2020). Using the tool Kaplan-Meier Plotter (Győrffy, 2021) to associate miR-2392 expression with pan-cancer patient survival (**Fig. S7**), a high expression of miR-2392 was generally related to poor prognosis with the majority of cancer types ($p<0.05$). Intriguingly, one miR-2392 predicted consequence was decreased antibody levels in the blood; this might account for the reported loss of the antibodies overtime (Gudbjartsson et al., 2020; Self et al., 2020).

Finally, using computational models we predicted small molecules, including FDA-approved drugs, that could inhibit miR-2392. First, a state-of-the-art machine learning algorithm for predicting missing drug targets (Galeano et al., 2021) was applied to an association dataset between 213 small molecules and 1,519 miRNAs from the SM2miR database (Liu et al., 2013) (see statistics in **Fig. S8**) integrating chemical and sequence similarity respectively. The average area under the ROC was of 0.877 when predicting missing small molecule-miRNA associations (**Fig. S9**). The top-20 predicted small molecules (**Fig. 7B**) includes Dexamethasone (Ledford, 2020) and Atorvastatin, that have shown protective roles in COVID-19 patients (Rossi et al., 2020). Second, following the ideas first presented in Sirota *et al.* (Sirota et al., 2011), we performed an analysis on the genomic signature of miR-2392 (*i.e.* significant up and down-regulated genes)

and predicted small molecules that can reverse it. We screened the genomic signatures of miR-2392 against 30,000 small molecules contained in the connectivity map (CMAP) (Lamb et al., 2006). The top-20 predicted small molecules includes the androgen receptor antagonist Enzalutamide and the insulin sensitizer Pioglitazone (Carboni et al., 2020) both of which are in clinical trials for COVID-19 (**Fig. 7C;** Clinical Trial NCT04475601 and NCT04604223). We also found literature evidence for leukotriene inhibitor ubenimex (Asai et al., 2020), and bacterial DNA inhibitor metronidazole (Gharebaghi et al., 2020).

Discussion

While the potential eradication of the novel coronavirus through worldwide vaccination is underway, new potent strains of SARS-CoV-2 are constantly evolving and there remains a major need to develop effective interventional strategies to minimize the damage caused by coronavirus infections. Host-mediated lung inflammation is a driver of mortality in COVID-19 critically ill patients. Thus, it is logical to focus on therapeutics that may have immunomodulating properties or disrupt viral replication. Our research uncovers a novel eight miRNA signature in patients with COVID-19 viral loads compared to those without disease as predicted from RNA-seq data. The expression of seven miRNAs was decreased (miR-10, miR-1, miR-34a-5p, miR-30c-5p, miR-29b-3p, miR-124-3p, and miR-155-5p) while a single miRNA, miR-2392, was significantly increased (**Fig. 1**). This key miRNA signature was involved in major cellular and molecular mechanisms that drives the viral-host response.

Upregulation of miR-10a-5p led to suppression of SDC1 defending against Porcine hemagglutinating encephalomyelitis virus (Hu et al., 2020). Notably, upregulation of mir-30c-5p and miR-155-5p have been independently shown to be involved with antiviral functions through immune and inflammatory pathways with other coronaviruses (Dickey et al., 2016; Ma et al., 2018). Inhibition of miR-34a-5p in the host by SARS-CoV-2 suppresses beneficial antiviral pathways (Bartoszewski et al., 2020). MiR-1-3p has been identified as an antiviral agent for viral related respiratory diseases (Sardar et al., 2020). MiR-1-3p and miR-155-5p from serum samples were significantly inhibited (**Figs. S3 and S4**), in agreement with the literature above.

Several studies have measured differential expression of miRNAs in COVID-19 patients and proposed their use as biomarkers or therapeutics. Lung biopsies from 9 COVID-19 patients showed miR-26a, miR-29b, and miR-34a correlated to endothelial dysfunction and inflammatory biomarkers (Centa et al., 2020). Sequencing in the blood from moderate or severe COVID-19 patients identified miR-146a, miR-21, miR-142, and miR-15b as potential biomarkers as well as contributors to disease pathogenesis (Tang et al., 2020). While these studies are limited to a specific tissue, our data that correlates miRNA signatures from multiple tissues (**Fig. 3**) suggests miR-2392 is a unique target that is ubiquitously involved in COVID-19 symptoms. To start addressing the multi-tissue impact of miR-2392 we show that miR-2392 is overexpressed in healthy monocyte cells infected with both the reference and P1 SARS-CoV-2 variants (**Fig. 5D**). This can indicate isolated cells will overexpress miR-2392 when infected with SARS-CoV-2 and further work is currently being done to investigate multi-tissue behavior of miR-2392.

The majority of miR-2392 publications are focused on cancer tissues where it may drive cellular invasion and metastasis. MiR-2392 was one of 6 circulating miRNAs altered in the serum and tissue of patients with cervical cancer used to predict metastasis (Chen et al., 2013). Higher

levels of miR-2392 in gastric cancer was associated with lower clinical staging and increased patient survival (Li et al., 2017) by inhibiting invasion and metastasis through the loss of Snail1, Slug, and Twist1 expression. Similarly, lower miR-2392 and miR-1587 levels were found in human keloid tissues that resulted in a loss of inhibition of ZEB2 and subsequent promotion of cellular proliferation and invasion (Hou et al., 2017). Inhibition of miR-2392 by the long-non-coding RNA CACNA1G-AS1 promoted hepatocellular carcinoma through disrupting the degradation of C1orf61, a tumor activator associated with metastasis and progression (Hu et al., 2013; Yang et al., 2019). Recently, a novel role for miR-2392 in tongue squamous cell carcinoma showed partial inhibition of transcription through direct miRNA-mtDNA base pairing resulting in reprogramming tumor cell metabolism and chemoresistance (Fan et al., 2019). These miR-2392 reports establish the significant impact this miRNA may have on cellular activity. Particularly relevant here is the more than 2-fold increase of miR-2392 in extracellular vesicles of Hepatitis B infected human hepatocytes (Enomoto et al., 2017). While miR-2392 has a reported impact on tumor cell biology, our study expands the valuable therapeutic potential of targeting miR-2392 to subsequently decrease SARS-CoV-2 viral infections (**Fig. 6**). These results warrant further exploration of the mechanistic underpinnings for the role of miR-2392 in driving viral infection.

One therapeutic insight deduced from miR-2392 interactions is the importance of the mitochondrial oxidative phosphorylation (OXPHOS) and glycolytic pathways in COVID-19, dramatically highlighted in BALF samples (**Fig. 1C**). In a study of tongue squamous cell carcinoma (Fan et al., 2019), miR-2392 enters the mitochondrion where it binds Ago2 and nucleotides 4379 to 4401 in the mtDNA heavy (H) strand within the MT-TQ (tRNA glutamine) gene (nucleotides m.4329-4400). MT-TQ is part of a large polycistronic transcript encompassing 12 of the mtDNA H strand polypeptide genes punctuated by tRNAs. Cleavage of the tRNAs releases the mRNAs. Upstream of MT-TQ are the 12S and 16S rRNAs and the complex I gene MT-ND1 gene. Downstream of MT-TQ is MT-ND2, MT-CO1, MT-CO2, MT-ATP6/8, MT-ND3, MT-ND4L, MT-ND4, MT-ND5, and MT-CYB (Lott et al., 2013; Wallace, 2018). Strikingly, the down-regulated mtDNA genes are the complex IV (cytochrome c oxidase) genes MT-CO1 and MT-CO2, the complex III (the bc_1 complex) gene (MT-CYB), and the complex I genes (MT-ND2, MT-ND4, and MT-ND5) (**Fig. 1C** right side arc). Since the miR-2392 inhibition of mtDNA OXPHOS genes (**Fig. 1C**) is also reflected in the down-regulation of the nuclear DNA coded mitochondrial transcripts of the complex I and IV genes and the iron-sulfur and heme iron complexes in the nasal, heart, and kidney autopsy samples (**Fig. 3D**), mitochondrial inhibition by miR-2392 appears to be the only physiological function that is common across all tissues in infected individuals suggesting mitochondrial modulation is a central feature of SARS-CoV-2 pathophysiology.

The inhibition of mitochondrial genes by miR-2392 would impair OXPHOS, which would have the most adverse effects on the high mitochondrial energetic tissues (brain, heart, kidney), the tissues central to the most severe COVID-19 cases. Inhibition of mitochondrial OXPHOS genes would increase mitochondrial reactive oxygen species (mROS) production, and induce glycolysis to compensate for the energy deficit (see top of **Fig 1C**). Mitochondrial function is regulated by the Sirtuins (Carrico et al., 2018), mitochondrial decline is associated with senescence, and mROS oxidation of mtDNA is linked to activation of the inflammasome and thus NFκB (West and Shadel, 2017; Zhong et al., 2018), all of which are modulated around miR-2392

(**Fig. 1C**). Thus, SARS-CoV-2 induction of miR-2392 (**Fig. 5**) and its associated inhibition of mtDNA and nuclear DNA OXPHOS genes (**Fig. 3** and **S1**) could explain many of the metabolic disturbances of COVID-19. Conversely, antagonism of miR-2392 function should ameliorate the inhibition of OXPHOS and may explain the therapeutic benefit of the anti-miR-2392 Nanoligomers.

Exploiting miRNAs from serum as a biomarker was pioneered in patients to examine diffuse large B-cell lymphoma (Lawrie et al., 2008). The use of miRNAs as a diagnostic biomarker has several advantages. Circulating miRNAs are readily obtained through a minimally invasive blood draw and are remarkably resistant to degradation in the plasma and serum (Mitchell et al., 2008). They may provide a means to detect asymptomatic individuals (Hou et al., 2017). However, potential confounding diseases that may influence the expression of multiple miRNAs requires the further evaluation of the targets found in this study (**Fig. 5**).

Advances in RNA chemistry and delivery systems enabled the first miRNA-based agents to enter into clinical trials several years ago (Rupaimoole and Slack, 2017). MiR-122 was found to increase the stability and replication of the Hepatitis C virus (HCV) through binding that prevented degradation by the Xrn1 exoribonuclease (Jopling et al., 2005; Thibault et al., 2015). Following a phase I clinical trial that inhibited miR-122 with no adverse reactions, a phase IIa trial showed a significant dose-dependent decrease in HCV load, one reported grade 3 thrombocytopenia, and only a small set of patients experienced viral rebound that might be linked to mutations of the HCV viral RNA (Janssen et al., 2013; Ottosen et al., 2015). A separate clinical trial targeting miR-122 reduced viral loads in all treated patients within 4 weeks with a sustained response in 3 patients after 76 weeks (van der Ree et al., 2017), however trials were suspended due to two cases of severe jaundice. These clinical trials have demonstrated the promising potential of using anti-miRNAs to significantly reduce viral infection with limited adverse effects and the similarities with miR-2392 with SARS-CoV-2 warrant further investigations to push to clinical trials.

Presently, there remains no specific treatment option for patients presenting with severe COVID-19 disease. While vaccines provide a promising avenue towards curbing the infection rate and minimizing symptoms, there remains an urgency to successfully develop and implement therapeutic agents to reduce severe consequences and subsequent patient mortality from COVID-19. As the testing of antibody-based or drug targeted therapies are currently underway, miRNAs represents a novel category of therapeutic agents that have previously shown endogenous activity to alter viral infection.

Acknowledgments: This work was supported by supplemental funds for COVID-19 research from Translational Research Institute of Space Health through NASA Cooperative Agreement NNX16AO69A (T-0404 to A.B. and T-0406 to A.C.) and further funding from KBR, Inc provided to A.B; this work used resources services, and support provided via the COVID-19 HPC Consortium (https://covid19-hpc-consortium.org/), provided specifically by the NASA High-End Computing (HEC) Program through the NASA Advanced Supercomputing (NAS) Division at Ames Research Center which was awarded to A.B.; DOD W81XWH-21-1-0128 awarded to D.C.W.; NIGMS P20 GM1009005 awarded to N.A.; Individual National Research Service Award F32-AI147587 awarded to J.M.D.; NIH/NHBLI K08 HL143271 and NIH/NHLBI R03 HL155249 awarded to R.S.H.; NIH/NCI U54 CA260543 supported R.S.H., N.M.B., M.C.W.; NSF 1956233 awarded to R.M.; A.P. was supported by Biotechnology and Biological Sciences Research Council

(https://bbsrc.ukri.org/) grants BB/K004131/1, BB/F00964X/1 and BB/M025047/1, Consejo Nacional de Ciencia y Tecnología Paraguay - CONACyT (http://www.conacyt.gov.py/) grants 14-INV-088 and PINV15-315, National Science Foundation Advances in Bio Informatics (https://www.nsf.gov/) grant 1660648; NSF IOS 1546858 to ESW; D.G. and A.P. were supported by the CONACyT grant PINV20-337 and the Fundação Getulio Vargas. N.M.B. was supported by the National Center for Advancing Translational Sciences (NCATS), NIH UL1TR002489, 2KR1272005, 550KR242003. P.M.M.V. was supported by FAPESP (grant numbers 20/04579-7, 16/18031-8); Fundo de Apoio ao Ensino, Pesquisa e Extensão (FAEPEX), Unicamp (grant number 2274/20); Coordenação de Aperfeiçoamento de Pessoal de Nível Superior - Brazil (CAPES) (Finance Code 001). Thanks to Dr. Richard Bowen for his assistance with the hamster studies and Dr. Matthew Frieman for his assistance with the *in vitro* A549 SARS-CoV-2 studies. Graphical abstract was created with BioRender.com partially adapted from "Bevacizumab: Potential Repurposed Drug Candidate for COVID-19" retrieved from https://app.biorender.com/biorender-templates.

Author contributions

Conceptualization: A.B.; Methodology: A.B.; Formal Analysis: A.B., R.M., C.V., D.T., F.J.E., C.M., C.M., J.C.S., J.T.M., J.M.D., D.G., U.S., E.S.W., A.S., J.F., V.Z., N.S., T.J.T.; Investigation: A.B., C.V., R.M., C.E.M., A.C., P.N., S.L.M., A.Y., T.R.A., P.M.M.V., G.G.D.; Sample Collection: M.M.S., M.C.W., R.S.H., N.M.B., U.C.P.C., A.D.H., J.C. P.M.M.V., G.G.D.; Resources: A.B., R.M., C.E.M., A.C., M.S., M.F., M.C.W.; Writing – Original Draft: A.B., J.T.M.; Writing – Review & Editing: A.B., J.T.M., F.J.E., R.J.G., W.P., M.M.S., J.M.D., J.W.G., D.W., S.S., S.B., V.Z., E.S.W., S.V.C., N.A, A.P., D.G., P.M.C., M.R.E., J.C.S., A.C., R.M., N.S., T.J.T., B.C., L.N.S., M.C.W., P.M.M.V.; Visualization: A.B., J.S.C, F.J.E, D.G., N.S., V.Z.; Supervision: A.B.; Funding Acquisition: A.B.

Declaration of Interests

A.C., P.N., S.V.C., A.B. have a provisional patent based on the antiviral discovery and design. A.C., P.N. and S.S. are part of the company (Sachi Bioworks Inc.) that has filed a patent on the Nanoligomer technology.

Figure Legends

Figure 1. Key miRNA signature as predicted from Bronchial Alveolar Lavage Fluid (BALF) RNA-seq data in patients with COVID-19. A) Predicted upstream regulators determined through Ingenuity Pathway Analysis (IPA) consistent with the transcriptional response from differentially expressed genes (FDR<0.05; outer ring). Eight miRNAs were among the key regulators in response to COVID-19 (inner ring). **B)** Major biological responses resulting from dysregulation of this eight miRNA signature drive immune- and inflammatory-related pathways as well as mitochondrial dysfunction determined through IPA. **C)** Pathway regulation by miR-2392 from BALF RNA-seq data determined through IPA.

Figure 2. Cross-species and viral integration of miR-2392. A) The conservation of miR-2392 across species determined by UCSC Genome Browser. Boxes (■) represent aligning and conserved sequence regions. Double horizontal line (=) represents both the genome and query have

unalignable sequence between regions of aligned sequence, a double-sided insertion. Single lines (-) indicate gaps. **B)** The expression of MEG3, the miR-2392 host gene, in different tissues from healthy patients. **C)** Potential binding sites of miR-2392 visualized across the SARS-CoV-2 genomes (NC045512.2 reference and lineages of concern from GISAID). Average miRanda scores are for hits within the 100bp window. Three top hits are shown.

Figure 3. Gene targets of miR-2392 in COVID-19 patients as well as mitochondrial and inflammatory genes. Volcano plots for differential gene expression from **A)** nasopharyngeal swab and autopsy COVID-19 patient tissues from the **B)** heart, **C)** kidney, **D)** liver, **E)** lung, and **F)** lymph node separated by viral load. **G)** Heatmaps display the t-score statistics when comparing viral load versus negative patient samples for nasopharyngeal swab and autopsy tissues. Main gene clusters were determined through k-mean clustering and annotated using ShinyGO (Ge et al., 2020) above the heatmap. MiR-2392 gene targets for **H)** mitochondrial specific genes or **I)** inflammatory genes are displayed. Genes shown have at least one comparison with an adjusted p-value (FDR<0.05) when comparing COVID-19 patients (high, medium or low viral loads) to non-infected control patients (none). Heatmaps from targets determined only from miRmap for miR-2392 mitochondrial or inflammatory gene targets are available in **Fig. S1**. or **Fig. S2**, respectively. **J)** Scatter plot of log_2-transformed fold changes in RNA and protein for miR-2392 targets for genes differentially expressed at the RNA level. Student's t-test, RNA p-value<=0.05, no limitation on protein p-value. **K)** Scatter plot of log_2-transformed medians in RNA and protein. COVID-19 positive (orange) or negative samples (grey). Student's t-test is used in fold change calculations. Size and opacity of the shape represent RNA fold change values. Shape represents fold change direction: circle = positive, triangle = negative. Pearson correlations are displayed in the top corner.

Figure 4. Increased miR-2392 expression *in vitro* mimics a COVID-19 disease phenotype. A-F) RNA-seq volcano plots in cells overexpressing miR-2392. **G-J)** Correlation plot between miR-2392 overexpression and related SARS-CoV-2 datasets. Circle size is proportional to the correlation coefficient. Statistical significance determined using a two-tailed Student's t-test *p<0.05, **p<0.01, ***p<0.001. **K-O**) Dot plots for statistically significant gene sets determined by fGSEA. NES, nominal enrichment score. **P)** and **Q)** Predicted miR-2392 targets by the MIRDIP algorithm that are downregulated in the overexpression experiments. The putative miR-2392 mRNA targets belonging to the consensus transcriptomic networks observed in SARS-CoV-2, MERS and Influenza infections of different human cells are represented in a Venn diagram in the upper part of the panel **P**.

Figure 5. Circulating miR-2392 with COVID-19 patients compared to COVID-19 negative patients. Droplet digital PCR (ddPCR) for miR-2392 on serum, urine, and nasopharyngeal swab samples (including seasonal coronavirus) from COVID-19 positive and negative patients. **A)** MiR-2392 levels from positive (SARS-CoV-2) or negative (neg) patients. Unadjusted t-tests for each tissue or adjusted statistics with a mixed model corrected for age and sex are shown. **B)** ROC curve for miR-2392 in each tissue. **C)** Tissue comparisons for multiple categories . N = COVID-19 Negative, P = COVID-19 positive, P_{int} = intubated patients, outp = outpatient, ICU = Intensive care unit/inpatient, Cold = common cold coronaviruses , NL63 = NL63 coronavirus and CoV-2 =

SARS-CoV-2. For all plots *p<0.05, **p<0.01, and ***p<0.001. **D)** MiR-2392 in monocytes from healthy donors (n=3) infected with SARS-CoV-2 reference strain and P1 variant. Comparisons with three other miRNAs were made with miR-1-3p (**Fig. S3**), miR-155-5p (**Fig. S4**), and miR-124-3p (**Fig. S5**).

Figure 6. Anti-miR-2393 therapeutic mitigation of SARS-CoV-2 infection with *in vitro* and *in vivo* models. A) Platform schematic for the miR-2392 inhibitor. **B–G)** Anti-miR-2392 Nanoligomers inhibitor or **E–G)** nonsense control applied to A549 cells infected with SARS-CoV-2 and tested for viral viability and cytotoxicity as biological replicates (n=3). **H–J)** Toxicity and efficacy of anti-miR-2392 Nanoligomers inhibitor in an *in vivo* infection hamster model. Treatments groups: SBCov207 by IP injection or IN instillation 24 hours prior to viral inoculation (IP or IN Day -1), 24 hours prior and post-viral challenge (IP or IN Day -1, +1), and 100ul of PBS 24 hours prior and post-viral challenge through IN instillation (PBS IN Day -1, +1). **H)** Pooled weights for each treatment group (n = 6 for days 1 – 3 and n = 3 for days 4 -7) as the maximum percent weight loss. **I)** SARS-CoV-2 assayed by plaque assay on Vero E6 cells from oropharyngeal swabs (N=6). **J)** Histopathological total score for lung tissues at day 3. Intranasal (IN), intraperitoneal (IP).

Figure 7. Predicted impact of miR-2392 on human disease and the top-20 drug compounds predicted to affect miR-2392 expression through machine learning approach. **A)** Dot plot of manually curated diseases associated with miR-2392 predicted from miR-2392 gene targets by miRnet. Values are plotted by p-value and dot size represents the number of downstream gene targets associated with disease. MiR-2392 expression related to patient survival in a pan-cancer analysis is highlighted in **Fig. S7**. **B)** Barplot of scores using our matrix completion model to predict small molecules that affect miRNA expression. Higher scores indicate more predicted associations. **C)** Barplot of the normalized connectivity map (CMAP) scores. We used transcripts induced by miR-2392 overrepresented genes to query CMAP. Higher negative scores reflect a greater reversal of the miR-2392 transcriptomic signature. Further details on model statistics and performance are found in **Figs. S8 – S10**.

Supplemental Figures and Material

The UNC COVID-19 Pathobiology Consortium is comprised of:

Shannon M Wallet[1,2], Robert Maile[2,3], Matthew C Wolfgang[2,4], Robert S Hagan[4,5], Jason R Mock[4,5], Natalie M Bowman[6], Jose L Torres-Castillo[5], Miriya K Love[5], Suzanne L Meinig[4], Will Lovell[1], Colleen Rice[5], Olivia Mitchem[1], Dominique Burgess[1], Jessica Suggs[1], Jordan Jacobs[3]

[1]Department of Oral and Craniofacial Health Sciences, UNC Adams School of Dentistry, University of North Carolina School of Medicine, Chapel Hill, NC, 27599, USA

[2]Department of Microbiology & Immunology, University of North Carolina School of Medicine, Chapel Hill, NC, 27599, USA

[3]Department of Surgery, University of North Carolina School of Medicine, Chapel Hill, NC, 27599, USA

[4]Marsico Lung Institute, University of North Carolina at Chapel Hill, Chapel Hill, NC, 27599, USA
[5]Division of Pulmonary Diseases and Critical Care Medicine, Department of Medicine, University of North Carolina, Chapel Hill, NC 27599, USA
[6]Division of Infectious Disease, School of Medicine, University of North Carolina, Chapel Hill, NC, 27599, USA

Figure S1. Mitochondrial gene targets of miR-2392 and regulated pathways. Related to Figure 3. Differential gene expression analysis for all miR-2392 mitochondrial gene targets significantly expressed in nasopharyngeal swab and autopsy COVID-19 patient tissues. The heatmaps display the t-score statistics for comparing viral load vs negative patient sample for all samples. Main gene clusters were determined through k-mean clustering. Nine main gene clusters were determined and ShinyGO (Ge et al., 2020) was utilized to determine the pathways for each cluster which are displayed on the top panel of the heatmap. Differentially expressed genes are shown with at least one comparison demonstrating a significant adjusted p-value (FDR<0.05) when comparing COVID-19 patients (high, medium or low viral loads) to non-infected control patients (none). Mir-2392 gene targets only determined from miRmap.

Figure S2. Inflammatory gene targets of miR-2392 and regulated pathways. Related to Figure 3. Differential gene expression analysis for all miR-2392 inflammatory gene targets significantly expressed in nasopharyngeal swab and autopsy COVID-19 patient tissues. The heatmaps display the t-score statistics for comparing viral load vs negative patient sample for all samples. Main gene clusters were determined through k-mean clustering. Eight main gene clusters were determined and ShinyGO (Ge et al., 2020) was utilized to determine the pathways for each cluster which are displayed on the top panel of the heatmap. Differentially expressed genes are shown with at least one comparison demonstrating a significant adjusted p-value (FDR<0.05) when comparing COVID-19 patients (high, medium or low viral loads) to non-infected control patients (none). Mir-2392 gene targets only determined from miRmap.

Figure S3. Circulating miR-1-3p with COVID-19 patients compared to COVID-19 negative patients. Related to Figure 5. Droplet digital PCR (ddPCR) with specific primer for miR-1-3p was performed on serum, urine, and nasopharyngeal swab samples (including other seasonal coronavirus samples) from COVID-19 positive and negative patients. The miRNA concentration are reported as copies/5ng RNA. **A)** The levels of miRNA-2392 in all tissues from patients grouped as SARS-CoV-2 positive (SARS-nCoV-2) or negative (neg). Unadjusted t-tests comparing the SARS-CoV-2 positive to neg for each tissue are provided and also adjusted statistics comparing the groups with a mixed model corrected for age and sex is provided. **B)** Receiver Operating Characteristic (ROC) curve is provided for miR-1-3p for each tissue comparing SARS-CoV-2 positive to negative patients. **C)** Comparing specific categories within each tissue type between COVID-19 positive and negative patients. N = COVID-19 Negative, P = COVID-19 positive, P_{int} = intubated patients, outp = outpatient, ICU = Intensive care unit/inpatient, Cold = Coronaviruses related to the common cold, NL63 = NL63 coronavirus, and CoV-2 = SARS-CoV-2. **D)** The levels of miR-1-3p in monocytes from healthy donors (n = 3) that were infected with SARS-CoV-2

reference strain and P1 variant. Triplicate conditions were done for each donor. For all plots * = $p < 0.05$, ** = $p < 0.01$, and *** = $p < 0.001$.

Figure S4. Circulating miR-155-5p with COVID-19 patients compared to COVID-19 negative patients. Related to Figure 5. Droplet digital PCR (ddPCR) with specific primer for miR-155-5p was performed on serum, urine, and nasopharyngeal swab samples (including other seasonal coronavirus samples) from COVID-19 positive and negative patients. The miRNA concentration are reported as copies/5ng RNA. **A)** The levels of miRNA-2392 in all tissues from patients grouped as SARS-CoV-2 positive (SARS-nCoV-2) or negative (neg). Unadjusted t-tests comparing the SARS-CoV-2 positive to neg for each tissue are provided and also adjusted statistics comparing the groups with a mixed model corrected for age and sex is provided. **B)** Receiver Operating Characteristic (ROC) curve is provided for miR-155-5p for each tissue comparing SARS-CoV-2 positive to negative patients. **C)** Comparing specific categories within each tissue type between COVID-19 positive and negative patients. N = COVID-19 Negative, P = COVID-19 positive, P_{int} = intubated patients, outp = outpatient, ICU = Intensive care unit/inpatient, Cold = Coronaviruses related to the common cold, NL63 = NL63 coronavirus, and CoV-2 = SARS-CoV-2. For all plots * = $p < 0.05$, ** = $p < 0.01$, and *** = $p < 0.001$.

Figure S5. Circulating miR-124-3p with COVID-19 patients compared to COVID-19 negative patients. Related to Figure 5. Droplet digital PCR (ddPCR) with specific primer for miR-124-3p was performed on serum, urine, and nasopharyngeal swab samples (including other seasonal coronavirus samples) from COVID-19 positive and negative patients. The miRNA concentration are reported as copies/5ng RNA. For miR-124-3p, the copies/5ng were either equal to 0 or at extremely low levels close to 0 copies/5ng. To try to determine any statistical differences we categorized the groups as ND = Not Determined which are all 0 values or D = Determined which are values > 0 for both N = negative (open symbols) and P = COVID-19 positive patients samples (closed symbols). The number of patients for each column is shown above the points. No significant differences were observed for any of the sample for miR-124-3p.

Figure S6. miR-2392 expression pan-cancer survival analysis. Related to Figure 7. Kaplan Meier patient survival plots for miR-2392 expression in a pan-cancer analysis was determined utilizing The Kaplan Meier plotter (Nagy et al., 2021). The plots were separated with the top row being cancers which patients had significantly poor survival with high expression of miR-2392, the middle row being cancers which patients had poor survival (but not significant) with high expression of miR-2392, and the bottom row being cancers which patients had significantly better survival with high expression of miR-2392.

Figure S7. Small molecules-miRNA dataset statistics Related to Figure 7. (Left) Number of small molecules associated to miRNAs. (Right) Number of miRNAs associated to small molecules.

Figure S8. Performance of our method at predicting missing small molecule-miRNA interactions. Related to Figure 7. (Top) The mean value of the Receiver Operating Curve (ROC)

is shown for a ten-fold cross-validation experiment (dark blue). 95% confidence interval is also shown (light blue). (Bottom) The mean value of the Precision-Recall Curve (PRC) is shown for a ten-fold cross-validation experiment (dark salmon). 95% confidence interval is also shown (light salmon).

Figure S9. Performance of our method at predicting missing small molecule-miRNA interactions when controlling for data imbalance. Related to Figure 7. (Top) Area Under the Receiver Operating Curve (AUROC) was obtained in a ten-fold cross-validation experiment for varying values of the negative to positive label ratio in the test set. (Bottom) Area Under the Precision-Recall Curve (AUROC) was obtained in a ten-fold cross-validation experiment for varying values of the negative to positive label ratio in the test set.

Table S1. Annealing temperatures for miRNA primers, related to methods and Figure 5. Temperatures used for droplet digital PCR to quantify each miRNA target.

STAR★Methods

RESOURCE AVAILABILITY

Lead Contact

Further information and requests for resources and reagents should be directed to and will be fulfilled by the Lead Contact, Afshin Beheshti (afshin.beheshti@nasa.gov).

Materials Availability

This study did not generate new unique reagents.

Data and Code Availability

The published article includes all datasets generated and analyzed during this study. Processed bulk RNA-seq data is available online (https://covidgenes.weill.cornell.edu/).

EXPERIMENTAL MODEL AND SUBJECT DETAILS

Human serum and nasopharyngeal swab sample collection for ddPCR

All plasma and nasal swab samples from those with COVID-19 infection, seasonal coronavirus infection, and controls were collected from inpatients at the University of Maryland Medical Center, in Baltimore, USA, between March and May of 2020. Sample collection obtained through informed consent waiver, which was approved by the University of Maryland, Baltimore IRB.

For serum samples, N=10 samples from COVID-19 intubated patients, COVID-19 outpatients, and COVID-19 negative patients were obtained. An equal distribution of N=5 males and females were used for each group. Also, an equal age distribution of patients from 27 to 85 years old was utilized for each group.

For the nasopharyngeal samples the following patient samples were obtained: N=10 SARS-CoV-2 positive patients, N=6 common cold coronavirus samples, and N=6 Coronavirus NL63

samples. For the common cold coronavirus samples the breakdown was the following for the specific viruses: N=2 Coronavirus 229E, Coronavirus HKU1, and N=2 Coronavirus OC43.

Human nasopharyngeal swab sample collection for RNA-seq analysis

Patient specimens were processed as described in Butler et al., 2020 (Butler et al., 2021). Briefly, nasopharyngeal swabs were collected using the BD Universal Viral Transport Media system (Becton, Dickinson and Company, Franklin Lakes, NJ) from symptomatic patients. Total Nucleic Acid (TNA) was extracted from using automated nucleic acid extraction on the QIAsymphony and the DSP Virus/Pathogen Mini Kit (Qiagen).

Human autopsy tissue collection for RNA-seq analysis

The full methods of the patient sample collection from the autopsy patients are currently available in the Park et al. (Park et al., 2021). All autopsies are performed with consent of next of kin and permission for retention and research use of tissue. Autopsies were performed in a negative pressure room with protective equipment including N-95 masks; brain and bone were not obtained for safety reasons. All fresh tissues were procured prior to fixation and directly into Trizol for downstream RNA extraction. Tissues were collected from lung, liver, lymph nodes, kidney, and the heart as consent permitted. For GeoMx, RNAscope, trichrome and histology tissue sections were fixed in 10% neutral buffered formalin for 48 hours before processing and sectioning. These cases had a post-mortem interval of less than 48 hours. For bulk RNA-seq tissues, post-mortem intervals ranged from less than 24 hours to 72 hours (with 2 exceptions - one at 4 and one at 7 days - but passing RNA quality metrics) with an average of 2.5 days. All deceased patient remains were refrigerated at 4ºC prior to autopsy performance.

Human urine sample collection

Urine was collected from patients and volunteers at the University of North Carolina at Chapel Hill. All patients provided informed consent prior to participation in IRB-approved research protocols (UNC IRB: 20-0822 [RHS] and 20-0792 [NMB]). Mid-stream urine of outpatients and non-critically ill patients was collected by the clean catch method. Urine of intubated critically ill patients was collected from a port on the Foley catheter. Urine was aliquoted into 5 ml aliquots and stored at -80°C.

Urine aliquots were thawed, and microRNA was extracted from 1 ml per sample using Norgen Urine microRNA Purification Kit (Cat. 29000). Microalbumin and creatinine levels were assessed using Microalbumin 2-1 Combo strips (CLIAwaived Inc, cat# URS-2M).

Human peripheral blood mononuclear cells collection for ddPCR

Peripheral blood mononuclear cells (PBMC) were obtained from buffy coats (Hematology and Hemotherapy Center of the University of Campinas) from healthy donors provided Study was approved by the Brazilian Committee for Ethics in Human Studies (CAEE: 31622420.0.0000.5404). PBMCs were isolated as described in Codo et al. (Codo et al., 2020).

Cell lines used for miR-2392 mimic experiments

Human SH-SY5Y cells were obtained from the ATCC and grown in Minimum Essential Medium (Gibco) / 10% FBS (Invitrogen) /1% MEM Non Essential Amino Acids (Gibco) /

1%GlutaMAX -l (Gibco). Cells were plated in 3.5 cm dishes and incubated with miR-2392 or control lentivirus particles (MOI 1) for 48h. Cells were harvested and lysed in Trizol reagent and RNA was extracted following manufacturers protocol (Invitrogen).

COVID-19 hamster model

Male Syrian hamsters 6-8 weeks old were utilized for efficacy studies with anti-miR-2392 Nanoligomers treatment. Three hamsters were used for each experimental group for a total of 30 hamsters with 10 treatment groups. Hamsters were infected with 10^5 pfu of the WA01/2020 strain of SARS-CoV-2 passaged twice in Vero E6 cells from the original isolate obtained from BEI Resources. There were 5 major treatment groups (N=6 per group) with two endpoints at day 3 or 7 post-viral challenge (N=3 per endpoint). Groups 1 and 3 were given the Nanoligomer treatment by Intraperitoneal (IP) injection while groups 2 and 4 were given by Intranasal (IN) instillation under ketamine-xylazine anesthesia. Groups 1 and 2 were given single Nanoligomer treatment 24 hours before viral challenge. Groups 3 and 4 were given two doses of Nanoligomer at 24 hours before and 24 hours after viral challenge. The control group 5 was treated with PBS 24 hours prior to and 24 hours following viral challenge by IN instillation. A primary focus for the animal tests was to assess treatment efficacy to reduce viral infection in the pulmonary system. Thus, the Nanoligomers were administered directly to lung tissues via the IN route and the primary endpoints were specifically evaluated for oropharyngeal shedding of virus and lung tissue burden for the virus at necropsy. Injecting the Nanoligomer intravenously (IV) may have also provided a suitable route to target the pulmonary system, however there is concern that the blood filtering organs or uptake in the endothelium may have blunted delivery directly to the lungs.

Treatment efficacy was assessed in multiple ways: 1) Change in daily body weight, 2) oropharyngeal shedding of virus on days 1-3 from all groups post-challenge assayed by plaque assay on Vero E6 cells (PFU/swab), 3) tissue burden of the virus at necropsy on day 3 from 2 lung tubes and turbinates assayed by plaque assay (PFU/100mg), and 4) histopathologic scoring on lungs and turbinates from all hamsters; the histopathological score for individual tissues, inflammation score from the interstitial lung inflammation, and total histopathological scores/assessment was made.

The dose of anti-miR-2392 that was used was calculated to raise blood levels to 10 μM if it were given intravenously. The dose was estimated from the average IC50s determined from our *in vitro* viral screening experiments. The molecular weight of anti-miR-2392 is 15,804. Assuming that hamsters weigh 120 grams and have 8% of body weight as blood, blood volume was approximately 0.01 liters. The dose per hamster was 1.58 mg in a 100 μl volume from an anti-miR-2392 solution.

In vitro viral screening model

A549-ACE2 cells, gifted by Dr. Brad Rosenberg (MSSM), were maintained in DMEM (Quality Biological, Gaithersburg, MD; #112-014-101) + 10% Fetal Bovine Serum (Gibco; #26140079) + 1% Penicillin-Streptomycin (Gemini Bio; #400-109). The day prior to treatment, 5,000 A549-ACE2 cells were plated per well in 96-well plates. MiR-2932 was diluted in duplicate in A549-ACE2 media to a starting concentration of 20μM (Run 1) or 22μM (Runs 2 and 3), and then an 8-point 1:2 dilution series was prepared. Media was removed from cells and 90μL of each

dilution was transferred to the cells. The plates were incubated for 2 hours at 37°C before being infected with an M.O.I. of 0.1 SARS-CoV-2 WA-1 (provided by Dr. Natalie Thornburg at the Centers for Disease Control and Prevention). Parallel plates were also run and left uninfected to monitor toxicity. Since Runs 2 and 3 were run simultaneously, a single toxicity plate was run for both. All plates were incubated at 37°C for 72 hours before being analyzed via Cell Titer Glo (Promega, Madison, WI; #G7573). Cell viability was compared to uninfected, untreated cells and infected, untreated cells.

METHOD DETAILS

Human peripheral blood mononuclear cell infection with SARS-CoV-2

Monocytes were isolated from PBMCs as described in Toniolo et al. (Toniolo et al., 2015). Cells were infected with SARS-CoV-2 B and P1 lineages as described. B lineage virus was isolated from the second confirmed case in Brazil (GenBank: MT126808.1). P1 was obtained as described by Souza et al. (Souza et al., 2021).

miRNA extraction for Droplet Digital PCR (ddPCR)

MiRNA extractions from serum were carried out using the Qiagen miRNeasy serum/plasma kit (#217184). MiRNA extractions from urine samples were carried out using Norgen urine microRNA Purification Kit (Cat. 29000, Norgen Bioteck Corp. Thorold, ON, Canada). Quantitation of miRNA samples was done using a NanoDrop 2000 Spectrophotometer (ThermoFisher Scientific).

cDNA generation and ddPCR

First, cDNA was synthesized from miRNA samples using the Qiagen miRCURY LNA RT Kit (Cat. 339340) using a concentration of 5ng/μl for the miRNA per sample. Next, samples were mixed with a 1:20 dilution of the generated cDNA with the BioRad QX200 ddPCR Evagreen Supermix (Cat. 1864034) and the appropriate miRNA primers from miRCURY LNA miRNA PCR Assays (Qiagen). BioRad QX200 Automated Droplet Generator (Cat. 1864101) was used to create emulsion droplets. With the C1000 Touch™ Thermal Cycler with 96–Deep Well Reaction Module (Bio-Rad) the following PCR reaction was used for all the primers: 1 cycle 95°C for 5 min, 40 cycles of 95°C for 30 sec and 58°C for 1 min (the annealing temperature can change depending on the primer), 1 cycle of 4°C for 5 min, and 1 cycle of 90°C for 5 min. Not all miRNA primers sets for ddPCR will have the same annealing temperature, so optimizing the annealing temperature is required for each primer set. Their respective annealing temperatures are found in **Table S1**. Finally, the QX200™ Droplet Digital™ PCR System (Bio-Rad) quantified the amount of miRNA for each primer set per sample. QuantaSoft software (Bio-Rad) generated the data for each primer set and sample. The same threshold setting was used for all samples per primer set. The concentration (miRNA copies/μl) value generated by QuantaSoft was converted to miRNA copies/ng of serum. These values were used for all miRNA analysis. For all analysis the miRNA concentrations were $\log_2(x+1)$ transformed to allow for easy comparison between miRNAs and samples.

Publicly available Bronchial Alveolar Lavage Fluid (BALF) COVID-19 RNA-sequencing data

Fastq files were downloaded from SRA (NCBI BioProject PRJNA605907 (Shen et al., 2020) and NCBI BioProject PRJNA390194 (Ren et al., 2018)). Fastq data files were trimmed using TrimGalore v (0.6.4) with a quality cutoff of 30. Data were then aligned using STAR (v2.7.3) two pass mode to the Human reference genome (GRCh38 v99 downloaded 04-27-2020). Unaligned data were written to a fastq file, and then realigned to the GRCh38 reference genome using Bowtie 2 (v2.3.4.1), and output sam file converted to a bam file using samtools (v1.7). The resultant Bam files were merged, sorted, and read groups added using picard tools (v2.21.3).

Publicly available RNA-seq data: A549, Calu-3, NHBE, and COVID-19 lung biopsy

Raw RNA-seq read counts from the publication by Blanco-Melo *et al.* for the A549, Calu-3, and NHBE cell lines as well as post-mortem lung biopsies from two COVID-19 patients were downloaded from the Gene Expression Omnibus (series accession GSE147507) (Blanco-Melo et al., 2020).

RNA-seq of Nasopharyngeal Swab COVID-19 patient samples

RNA isolation and library preparation is fully described in Butler, et al. (Butler et al., 2021). Briefly, library preparation on the all nasopharyngeal swab samples' total nucleic acid (TNA) were treated with DNAse 1 (Zymo Research, Catalog # E1010). Post-DNAse digested samples were then put into the NEBNext rRNA depletion v2 (Human/Mouse/Rat), Ultra II Directional RNA (10 ng), and Unique Dual Index Primer Pairs were used following the vendor protocols from New England Biolabs. Kits were supplied from a single manufacturer lot. Completed libraries were quantified by Qubit or equivalent and run on a Bioanalyzer or equivalent for size determination. Libraries were pooled and sent to the WCM Genomics Core or HudsonAlpha for final quantification by Qubit fluorometer (ThermoFisher Scientific), TapeStation 2200 (Agilent), and qRT-PCR using the Kapa Biosystems Illumina library quantification kit.

RNA-seq of COVID-19 autopsy tissue samples

RNA isolation and library preparation is fully described in Park, et al. (Park et al., 2021). Briefly, autopsy tissues were collected from lung, liver, lymph nodes, kidney, and the heart and were placed directly into Trizol, homogenized and then snap frozen in liquid nitrogen. At least after 24 hours these tissue samples were then processed via standard protocols to isolate RNA. New York Genome Center RNA sequencing libraries were prepared using the KAPA Hyper Library Preparation Kit + RiboErase, HMR (Roche) in accordance with manufacturer's recommendations. Briefly, 50-200ng of Total RNA were used for ribosomal depletion and fragmentation. Depleted RNA underwent first and second strand cDNA synthesis followed by adenylation, and ligation of unique dual indexed adapters. Libraries were amplified using 12 cycles of PCR and cleaned-up by magnetic bead purification. Final libraries were quantified using fluorescent-based assays including PicoGreen (Life Technologies) or Qubit Fluorometer (Invitrogen) and Fragment Analyzer (Advanced Analytics) and sequenced on a NovaSeq 6000 sequencer (v1 chemistry) with 2x150bp targeting 60M reads per sample.

miR-2392 mimic experiments in SH-SY5Y cells and RNA-seq

RNA was dissolved in nuclease free water and concentration determined spectrometrically at 260nm using a Biotek plate reader (Biotek). 500ng RNA was used as input for a whole transcriptome library preparation (ThermoFisher Total RNA). Libraries were quantified using a bioanalyzer chip reader (nanoDNA chips: Aglient Technologies) and diluted to 100 pM final concentration. Barcoded libraries were combined and use to seed a OneTouch bead templating reaction (OneTouch2). Cloned libraries were enriched and loaded on 540 Ion Torrent chips. Data were sequenced using the Ion Torrent RNA-seq workflow. Unaligned Bam files were converted to fatsq and aligned to the Grch 38 reference genome using STAR Two pass approach (Dobin et al., 2013) to create gene count tables as described in Overbey et al. (Overbey et al., 2021)(script in supplementary).

Anti-miR-2392 Nanoligomer inhibitor design and construction

The Nanoligomer platform was used to design Nanoligomer inhibitors, which are composed of a nanobiohydrd molecule based on antisense peptide nucleic acid (PNA) moiety conjugated to nanoparticle for improved delivery and membrane transport. The PNA moiety was chosen to be 15 bases long (in order to maximize both solubility and specificity), which yielded six potential target sequences within the 20-nucleotide mature human miR-2392. These potential targets were screened using FAST for solubility, self-complementing sequences, and off-targeting within the human genome (GCF_000001405.26) and SARS-CoV-2 viral genome (NC_045512). The antisense sequence complementing miR-2392 nucleotides 2 to 16 (TCTCACCCCCATCCT) was chosen in order to minimize off-targeting while maximizing coverage of the miR-2392 seed region. The Nanoligomer was synthesized (with an N-terminal histidine tag and a 2-(2-(2-aminoethoxy)ethoxy)acetic acid linker) on an Apex 396 peptide synthesizer (AAPPTec, LLC) with solid-phase Fmoc chemistry. Fmoc-PNA monomers were obtained from PolyOrg Inc., with A, C, and G monomers protected with Bhoc groups. Following synthesis, the peptides were conjugated with nanoparticles and purified via size-exclusion filtration. Conjugation and concentration of the purified solution was monitored through measurement of absorbance at 260 nm (for detection of PNA) and 400 nm (for quantification of nanoparticles).

QUANTIFICATION AND STATISTICAL ANALYSIS

Analysis of BALF RNA-seq data

Bam files were imported into Partek Genome Studio v7.0, and gene expression values quantified vs the Grch38 reference annotation guide (Ensembl v99). Samples with fewer than 2 million aligned reads were excluded from further analysis. Genes with fewer than 10 reads in 25% of samples were excluded, and differential gene expression determined using ANOVA with infection status as contrast. Differentially expressed gene files were used in GSEA and IPA to determine biological significance and pathways being regulated.

Analysis of Nasopharyngeal Swab RNA-seq data

The nasopharyngeal swab samples were analyzed comparing COVID-19 viral infection to the negative patients and was as previously described in Butler et al. (Butler et al., 2021) and the DESeq2 (Love et al., 2014) was utilized to generate the differential expression data. Heatmaps

were displayed using pheatmap (Kolde, 2015). Volcano plots were made use R program EnhancedVolcano (Blighe et al., 2018).

Analysis of Autopsy RNA-seq data

The full methods of the analysis from the autopsy patients is currently available in the Park et al. (Park et al., 2021). Briefly, RNA-seq data was processed through the nf-core/rnaseq pipeline (Ewels et al., 2020). This workflow involved adapter trimming using Trim Galore! (https://github.com/FelixKrueger/TrimGalore), read alignment with STAR (Dobin et al., 2013), gene quantification with Salmon (Patro et al., 2017), duplicate read marking with Picard MarkDuplicates (https://github.com/broadinstitute/picard), and transcript quantification with StringTie (Kovaka et al., 2019). Other quality control measures included RSeQC, Qualimap, and dupRadar. Alignment was performed using the GRCh38 build native to nf-core and annotation was performed using Gencode Human Release 33 (GRCH38.p13). FeatureCounts reads were normalized using variance-stabilizing transform (vst) in DESeq2 package in R for visualization purposes in log-scale (Love et al., 2014). Differential expression of genes were calculated by DESeq2. Differential expression comparisons were done as either COVID+ cases versus COVID- controls for each tissue specifically, correcting for sequencing batches with a covariate where applicable, or pairwise comparison of viral levels from the lung as determined by nCounter data. Volcano plots were made use R program EnhancedVolcano (Blighe et al., 2018).

Analysis Combining Autopsy and Nasopharyngeal Swab RNA-seq data

To combine the results from the autopsy and nasopharyngeal swab RNA-seq data, we utilized the t-score values from the DESeq2 analysis. Heatmaps were displayed using pheatmap (Kolde, 2015).

Gene Set Enrichment Analysis (GSEA)

For pathway analysis on the miR-2392 targets (**Fig. 3**) we utilized ShinyGO (Ge et al., 2020) to determine the significantly regulated pathways for each main cluster in the heatmap. The clustering was determined through k-mean statistics.

For pathway analysis on the miR-2392 mimic RNA-seq data, we utilized fast Gene Set Enrichment Analysis (fGSEA) (Korotkevich et al., 2021). Pathway analysis was done comparing miR-2392 mimics to all controls and the ranked list of genes were defined by the t-score statistics. The statistical significance was determined by 1000 permutations of the genesets (Subramanian et al., 2005).

Analysis of proteomic and transcriptomic blood datasets from COVID-19 patients

For the analysis of the miR-2392 targets in the blood tissue, we downloaded whole blood transcriptome data and plasma proteome data from The COVIDome Explorer Researcher Portal (Sullivan et al., 2021). For Transcriptome data we used the following filters: Category "Effect of COVID-19 status", Platform "Blood", Statistical test "Student's t-test", Adjustment method "none", Sex "male" and "female", Age Group "All". For Proteome data we used the following filters: Category "Effect of COVID-19 status", Platform "SOMAscan", Statistical test "Student's t-test", Adjustment method "none", Sex "male" and "female", Age Group "All". We created the list of the

intersecting genes from both datasets. We analyzed the list using RStudio Desktop 1.3.1093 (RStudio Team (2020). RStudio: Integrated Development Environment for R. RStudio, PBC, Boston, MA URL http://www.rstudio.com/), and visualized data using ggplot2 version 3.3.2 (Wickham, 2016) and ggrepel version 0.8.2 (https://ggrepel.slowkow.com/).

Analysis of Monocyte RNA-seq data

The monocyte COVID-19 RNA-Seq data, published under the accession GSE159678 (Rother et al., 2020), was downloaded from SRA and gene expression was quantified using Salmon's selective alignment approach (Srivastava et al., 2020). The RNA-Seq processing pipeline was implemented using pyrpipe (Singh et al., 2021) (https://github.com/urmi-21/pyrpipe/tree/master/case_studies/Covid_RNA-Seq). Exploratory data analysis and differential expression analysis were performed using MetaOmGraph (Singh et al., 2020).

Analysis of A549, Calu-3, NHBE, and COVID lung biopsy data

Each data series was normalized and filtered for low-expressed genes (counts<1). Cell culture samples treated with SARS-CoV-2 were compared to untreated controls and COVID-19-positive patient samples were compared to healthy lung biopsies. Differentially expressed genes were determined from the R-program Limma-Voom (Ritchie et al., 2015) using a linear model with weighted least squares for each gene and the false discovery rate adjusted p-values were calculated.

Analysis of miR-2392 mimic RNA-seq data

Differential gene expression was determined using LIMMA-voom (Ritchie et al., 2015). Data were filtered to ensure data contained at least 5 million aligned reads, and average gene counts of > 10. Cell treatments we used as contrasts for differentially expressed gene calculations. These results were then uploaded to GSEA for further analysis. (R script in supplementary section)

Conservation of miR-2392 between species

To determined conservation of miR-2392 among different species we utilized UCSC Genome Browser (Kent et al., 2002). Hsa-miR-2392 was entered as input and target species were chosen to include common models for SARS-CoV-2 *in vivo* studies (e.g. mice, ferrets, and hamsters) as well as primates and other animals to provide a wide spectrum of species to observe conservation of miR-2392. The USCS Genome Browser provides the host gene for miR-2392 (i.e. MEG3) and redirects to GTEx (Consortium, 2020) to provide a plot of MEG3 levels based on RNA-seq data on normal tissues.

Mapping miR-2392 sequence to SARS-CoV-2 sequences

To explore potential binding sites for miR-2392 we used miRanda software (Enright et al., 2003) to identify all potential binding sites with respect to the SARS-CoV-2 reference genome (Wuhan-Hu-1; NC045512.2) and representative genomes from lineages of concern. The lineages of concern were selected from Global Initiative on Sharing All Influenza Data (GISAID) with each lineage being represented by 14 recent genomes.

In silico predictions of genes from miRNAs

Through the use of a Cytoscape (Shannon et al., 2003) plug-in called ClueGo/CluePedia (Bindea et al., 2009), we were able to predict genes targeted by the miRNAs determined. This involved entering all miRNAs in ClueGo and allowing the software to determine the top 50 genes that were significantly regulated and connected to the miRNAs. The predictions only reflect the functions that will be regulated by the miRNAs and do not show whether the function will be activated or inhibited. Lastly, miRNet 2.0 was utilized to predict the diseases and pathways that are associated with the miRNAs (Chang et al., 2020). This was plotted as a dot plot utilizing the R-program ggplot2 (v3.2.1) (Wickham, 2016).

ddPCR analysis of miRNA levels in patient samples

First, we normalized the amount of each miRNA measured per body location (nasal, serum, and urine) using the general logarithm transformation. We compared miRNA levels in samples from patients either positive or negative for SARS-nCoV-2 using the student's t-test (unadjusted) as well as controlling for sex and age using least squares adjustment. Next, we generated receiver operating characteristic curves from each body location to show the performance of a classification model (SARS-nCoV-2 positive versus negative) at all classification thresholds using the absolute, non-transformed levels (miRNA copies per 5 ng RNA). Finally, we performed a subanalysis on each location to compare the variance of each miRNA in SARS-nCoV-2 negative patients compared to other patient groups. For serum and nasal samples, 1-way ANOVA was used to identify variation associated with the patient classification. For urine samples, 2-way ANOVA was used with location (outpatient versus inpatient) and SARS-nCoV-2 positivity as the main factors. If the ANOVA yielded a $P < 0.05$, Dunnett's post-test was used to compare subgroup means to the negative patient sample mean.

Computational drug repositioning model

Using the SM2miR database (Lui et al., 2007), we assembled an $n \times m$ binary matrix (X) containing 3,593 associations between small molecules ($n = 213$, rows) and miRNAs ($m = 1{,}519$, columns). Each matrix entry (X_{ij}) was assigned a value of 1 where a small molecule is known to be associated to miRNA, and was 0 otherwise. The chemical notation as a simplified molecular input line entry system (SMILES) was obtained for each small molecule from PubChem. We then calculated the 2D Tanimoto chemical similarity between pairs of small molecules using the MACCS key binary fingerprints with RDKit (RDKit: Open-source cheminformatics; http://www.rdkit.org). Similarly, for each miRNA, we obtained its sequence from miRbase (Kozomara et al., 2019) and computed sequence similarity between miRNAs as the score of their Needleman-Wunsch alignment. We used the binary matrix, together with the chemical and sequence similarities, as input to our state-of-the-art drug target prediction model to predict missing associations in X (Galeano et al., 2021). The model parameters where: $p = ½$, $\beta_{Chem} = 1$, and $\alpha_{seq} = 0$. To assess the prediction performance of the model, we performed ten-fold cross-validation simulations.

References

Abdelrahman, Z., Liu, Q., Jiang, S., Li, M., Sun, Q., Zhang, Y., and Wang, X. (2021). Evaluation of the Current Therapeutic Approaches for COVID-19: A Systematic Review and a Meta-analysis. Front Pharmacol *12*, 607408.

Alamdari, D.H., Moghaddam, A.B., Amini, S., Keramati, M.R., Zarmehri, A.M., Alamdari, A.H., Damsaz, M., Banpour, H., Yarahmadi, A., and Koliakos, G. (2020). Application of methylene blue -vitamin C -N-acetyl cysteine for treatment of critically ill COVID-19 patients, report of a phase-I clinical trial. Eur J Pharmacol *885*, 173494.

Ardestani, A., and Azizi, Z. (2021). Targeting glucose metabolism for treatment of COVID-19. Signal Transduct Target Ther *6*, 112.

Asai, A., Konno, M., Ozaki, M., Otsuka, C., Vecchione, A., Arai, T., Kitagawa, T., Ofusa, K., Yabumoto, M., Hirotsu, T., *et al.* (2020). COVID-19 Drug Discovery Using Intensive Approaches. Int J Mol Sci *21*.

Aykin-Burns, N., Franklin, E.A., and Ercal, N. (2005). Effects of N-acetylcysteine on lead-exposed PC-12 cells. Arch Environ Contam Toxicol *49*, 119-123.

Baden, L.R., El Sahly, H.M., Essink, B., Kotloff, K., Frey, S., Novak, R., Diemert, D., Spector, S.A., Rouphael, N., Creech, C.B., *et al.* (2021). Efficacy and Safety of the mRNA-1273 SARS-CoV-2 Vaccine. N Engl J Med *384*, 403-416.

Bartoszewski, R., Dabrowski, M., Jakiela, B., Matalon, S., Harrod, K.S., Sanak, M., and Collawn, J.F. (2020). SARS-CoV-2 may regulate cellular responses through depletion of specific host miRNAs. Am J Physiol Lung Cell Mol Physiol *319*, L444-L455.

Bindea, G., Mlecnik, B., Hackl, H., Charoentong, P., Tosolini, M., Kirilovsky, A., Fridman, W.H., Pages, F., Trajanoski, Z., and Galon, J. (2009). ClueGO: a Cytoscape plug-in to decipher functionally grouped gene ontology and pathway annotation networks. Bioinformatics *25*, 1091-1093.

Blanco-Melo, D., Nilsson-Payant, B.E., Liu, W.C., Uhl, S., Hoagland, D., Moller, R., Jordan, T.X., Oishi, K., Panis, M., Sachs, D., *et al.* (2020). Imbalanced Host Response to SARS-CoV-2 Drives Development of COVID-19. Cell *181*, 1036-1045 e1039.

Blighe, K., Rana, S., and Lewis, M. (2018). EnhancedVolcano: Publication-ready volcano plots with enhanced colouring and labeling. https://github.com/kevinblighe/EnhancedVolcano.

Bojkova, D., Klann, K., Koch, B., Widera, M., Krause, D., Ciesek, S., Cinatl, J., and Munch, C. (2020). Proteomics of SARS-CoV-2-infected host cells reveals therapy targets. Nature *583*, 469-472.

Butler, D., Mozsary, C., Meydan, C., Foox, J., Rosiene, J., Shaiber, A., Danko, D., Afshinnekoo, E., MacKay, M., Sedlazeck, F.J., *et al.* (2021). Shotgun transcriptome, spatial omics, and isothermal profiling of SARS-CoV-2 infection reveals unique host responses, viral diversification, and drug interactions. Nat Commun *12*, 1660.

Carboni, E., Carta, A.R., and Carboni, E. (2020). Can pioglitazone be potentially useful therapeutically in treating patients with COVID-19? Med Hypotheses *140*, 109776.

Carfi, A., Bernabei, R., Landi, F., and Gemelli Against, C.-P.-A.C.S.G. (2020). Persistent Symptoms in Patients After Acute COVID-19. JAMA *324*, 603-605.

Carrico, C., Meyer, J.G., He, W., Gibson, B.W., and Verdin, E. (2018). The Mitochondrial Acylome Emerges: Proteomics, Regulation by Sirtuins, and Metabolic and Disease Implications. Cell Metab *27*, 497-512.

Centa, A., Fonseca, A.S., Ferreira, S., Azevedo, M.L.V., Vaz de Paula, C.B., Nagashima, S., Machado-Souza, C., Miggiolaro, A., Baena, C.P., de Noronha, L., *et al.* (2020). Deregulated miRNA expression is associated with endothelial dysfunction in post-mortem lung biopsies of COVID-19 patients. Am J Physiol Lung Cell Mol Physiol.

Chang, L., Zhou, G., Soufan, O., and Xia, J. (2020). miRNet 2.0: network-based visual analytics for miRNA functional analysis and systems biology. Nucleic Acids Res *48*, W244-W251.

Chen, J., Yao, D., Li, Y., Chen, H., He, C., Ding, N., Lu, Y., Ou, T., Zhao, S., Li, L., *et al.* (2013). Serum microRNA expression levels can predict lymph node metastasis in patients with early-stage cervical squamous cell carcinoma. Int J Mol Med *32*, 557-567.

Chen, Y., and Wang, X. (2020). miRDB: an online database for prediction of functional microRNA targets. Nucleic Acids Res *48*, D127-D131.

Codo, A.C., Davanzo, G.G., Monteiro, L.B., de Souza, G.F., Muraro, S.P., Virgilio-da-Silva, J.V., Prodonoff, J.S., Carregari, V.C., de Biagi Junior, C.A.O., Crunfli, F., *et al.* (2020). Elevated Glucose Levels Favor SARS-CoV-2 Infection and Monocyte Response through a HIF-1alpha/Glycolysis-Dependent Axis. Cell Metab *32*, 437-446 e435.

Consortium, G.T. (2020). The GTEx Consortium atlas of genetic regulatory effects across human tissues. Science *369*, 1318-1330.

Dickey, L.L., Worne, C.L., Glover, J.L., Lane, T.E., and O'Connell, R.M. (2016). MicroRNA-155 enhances T cell trafficking and antiviral effector function in a model of coronavirus-induced neurologic disease. J Neuroinflammation *13*, 240.

Dobin, A., Davis, C.A., Schlesinger, F., Drenkow, J., Zaleski, C., Jha, S., Batut, P., Chaisson, M., and Gingeras, T.R. (2013). STAR: ultrafast universal RNA-seq aligner. Bioinformatics *29*, 15-21.

Dweep, H., and Gretz, N. (2015). miRWalk2.0: a comprehensive atlas of microRNA-target interactions. Nat Methods *12*, 697.

Edmonds, C.E., Zuckerman, S.P., and Conant, E.F. (2021). Management of Unilateral Axillary Lymphadenopathy Detected on Breast MRI in the Era of Coronavirus Disease (COVID-19) Vaccination. AJR Am J Roentgenol.

Eller, K.A., Aunins, T.R., Courtney, C.M., Campos, J.K., Otoupal, P.B., Erickson, K.E., Madinger, N.E., and Chatterjee, A. (2021). Facile accelerated specific therapeutic (FAST) platform develops antisense therapies to counter multidrug-resistant bacteria. Commun Biol *4*, 331.

Enomoto, Y., Takagi, R., Naito, Y., Kiniwa, T., Tanaka, Y., Hamada-Tsutsumi, S., Kawano, M., Matsushita, S., Ochiya, T., and Miyajima, A. (2017). Identification of the novel 3' UTR sequences of human IL-21 mRNA as potential targets of miRNAs. Sci Rep *7*, 7780.

Enright, A.J., John, B., Gaul, U., Tuschl, T., Sander, C., and Marks, D.S. (2003). MicroRNA targets in Drosophila. Genome Biol *5*, R1.

Ewels, P.A., Peltzer, A., Fillinger, S., Patel, H., Alneberg, J., Wilm, A., Garcia, M.U., Di Tommaso, P., and Nahnsen, S. (2020). The nf-core framework for community-curated bioinformatics pipelines. Nat Biotechnol *38*, 276-278.

Fan, S., Tian, T., Chen, W., Lv, X., Lei, X., Zhang, H., Sun, S., Cai, L., Pan, G., He, L., *et al.* (2019). Mitochondrial miRNA Determines Chemoresistance by Reprogramming Metabolism and Regulating Mitochondrial Transcription. Cancer Res *79*, 1069-1084.

Feng, L., Yin, Y.Y., Liu, C.H., Xu, K.R., Li, Q.R., Wu, J.R., and Zeng, R. (2020). Proteome-wide Data Analysis Reveals Tissue-specific Network Associated with SARS-CoV-2 Infection. J Mol Cell Biol.

Friedman, R.C., Farh, K.K., Burge, C.B., and Bartel, D.P. (2009). Most mammalian mRNAs are conserved targets of microRNAs. Genome Res *19*, 92-105.

Galeano, D., Noto, S., Jimenez, R., and Paccanaro, A. (2021). Interpretable Drug Target Predictions using Self-Expressiveness. bioRxiv, 2021.2003.2001.433365.

Ge, S.X., Jung, D., and Yao, R. (2020). ShinyGO: a graphical gene-set enrichment tool for animals and plants. Bioinformatics *36*, 2628-2629.

Gharebaghi, R., Heidary, F., Moradi, M., and Parvizi, M. (2020). Metronidazole; a Potential Novel Addition to the COVID-19 Treatment Regimen. Arch Acad Emerg Med *8*, e40.

Gudbjartsson, D.F., Norddahl, G.L., Melsted, P., Gunnarsdottir, K., Holm, H., Eythorsson, E., Arnthorsson, A.O., Helgason, D., Bjarnadottir, K., Ingvarsson, R.F., *et al.* (2020). Humoral Immune Response to SARS-CoV-2 in Iceland. N Engl J Med *383*, 1724-1734.

Győrffy, B. (2021). Survival analysis across the entire transcriptome identifies biomarkers with the highest prognostic power in breast cancer. Computational and Structural Biotechnology Journal *19*, 4101-4109.

Hemmat, N., Asadzadeh, Z., Ahangar, N.K., Alemohammad, H., Najafzadeh, B., Derakhshani, A., Baghbanzadeh, A., Baghi, H.B., Javadrashid, D., Najafi, S., *et al.* (2021). The roles of signaling pathways in SARS-CoV-2 infection; lessons learned from SARS-CoV and MERS-CoV. Archives of Virology *166*, 675-696.

Herrmann, J., Mori, V., Bates, J.H.T., and Suki, B. (2020). Modeling lung perfusion abnormalities to explain early COVID-19 hypoxemia. Nat Commun *11*, 4883.

Ho, W.Z., and Douglas, S.D. (1992). Glutathione and N-acetylcysteine suppression of human immunodeficiency virus replication in human monocyte/macrophages in vitro. AIDS Res Hum Retroviruses *8*, 1249-1253.

Hou, X., Liang, Y., Chen, J., Wei, Y., Zeng, P., Wang, L., Lu, C., and Diao, H. (2017). Expression Profiling of Cellular MicroRNA in Asymptomatic HBsAg Carriers and Chronic Hepatitis B Patients. Biomed Res Int *2017*, 6484835.

Hu, H.M., Chen, Y., Liu, L., Zhang, C.G., Wang, W., Gong, K., Huang, Z., Guo, M.X., Li, W.X., and Li, W. (2013). C1orf61 acts as a tumor activator in human hepatocellular carcinoma and is associated with tumorigenesis and metastasis. FASEB J *27*, 163-173.

Hu, S., Li, Z., Lan, Y., Guan, J., Zhao, K., Chu, D., Fan, G., Guo, Y., Gao, F., and He, W. (2020). MiR-10a-5p-Mediated Syndecan 1 Suppression Restricts Porcine Hemagglutinating Encephalomyelitis Virus Replication. Front Microbiol *11*, 105.

Huang, C., Wang, Y., Li, X., Ren, L., Zhao, J., Hu, Y., Zhang, L., Fan, G., Xu, J., Gu, X., *et al.* (2020). Clinical features of patients infected with 2019 novel coronavirus in Wuhan, China. Lancet *395*, 497-506.

Hultstrom, M., Lipcsey, M., Wallin, E., Larsson, I.M., Larsson, A., and Frithiof, R. (2021). Severe acute kidney injury associated with progression of chronic kidney disease after critical COVID-19. Crit Care *25*, 37.

Ibrahim, H., Perl, A., Smith, D., Lewis, T., Kon, Z., Goldenberg, R., Yarta, K., Staniloae, C., and Williams, M. (2020). Therapeutic blockade of inflammation in severe COVID-19 infection with intravenous N-acetylcysteine. Clin Immunol *219*, 108544.

Islam, M.S., and Islam, A.B.M.M.K. (2021). Viral miRNAs confer survival in host cells by targeting apoptosis related host genes. Informatics in Medicine Unlocked *22*, 100501.

Jacobs, L.G., Gourna Paleoudis, E., Lesky-Di Bari, D., Nyirenda, T., Friedman, T., Gupta, A., Rasouli, L., Zetkulic, M., Balani, B., Ogedegbe, C., *et al.* (2020). Persistence of symptoms and quality of life at 35 days after hospitalization for COVID-19 infection. PLoS One *15*, e0243882.

Janssen, H.L., Reesink, H.W., Lawitz, E.J., Zeuzem, S., Rodriguez-Torres, M., Patel, K., van der Meer, A.J., Patick, A.K., Chen, A., Zhou, Y., *et al.* (2013). Treatment of HCV infection by targeting microRNA. N Engl J Med *368*, 1685-1694.

Jia, D., Koonce, N.A., Griffin, R.J., Jackson, C., and Corry, P.M. (2010). Prevention and mitigation of acute death of mice after abdominal irradiation by the antioxidant N-acetyl-cysteine (NAC). Radiat Res *173*, 579-589.

Jiang, Q., Wang, Y., Hao, Y., Juan, L., Teng, M., Zhang, X., Li, M., Wang, G., and Liu, Y. (2009). miR2Disease: a manually curated database for microRNA deregulation in human disease. Nucleic Acids Res *37*, D98-104.

Johansen, M.D., Irving, A., Montagutelli, X., Tate, M.D., Rudloff, I., Nold, M.F., Hansbro, N.G., Kim, R.Y., Donovan, C., Liu, G., *et al.* (2020). Animal and translational models of SARS-CoV-2 infection and COVID-19. Mucosal Immunol *13*, 877-891.

Jopling, C.L., Yi, M., Lancaster, A.M., Lemon, S.M., and Sarnow, P. (2005). Modulation of hepatitis C virus RNA abundance by a liver-specific MicroRNA. Science *309*, 1577-1581.

Kent, W.J., Sugnet, C.W., Furey, T.S., Roskin, K.M., Pringle, T.H., Zahler, A.M., and Haussler, D. (2002). The human genome browser at UCSC. Genome Res *12*, 996-1006.

Kolde, R. (2015). pheatmap: Pretty heatmaps [Software].

Korotkevich, G., Sukhov, V., Budin, N., Shpak, B., Artyomov, M.N., and Sergushichev, A. (2021). Fast gene set enrichment analysis. bioRxiv, 060012.

Koumpa, F.S., Forde, C.T., and Manjaly, J.G. (2020). Sudden irreversible hearing loss post COVID-19. BMJ Case Rep *13*.

Kovaka, S., Zimin, A.V., Pertea, G.M., Razaghi, R., Salzberg, S.L., and Pertea, M. (2019). Transcriptome assembly from long-read RNA-seq alignments with StringTie2. Genome Biol *20*, 278.

Kozomara, A., Birgaoanu, M., and Griffiths-Jones, S. (2019). miRBase: from microRNA sequences to function. Nucleic Acids Res *47*, D155-D162.

Krajewski, P.K., Maj, J., and Szepietowski, J.C. (2021). Cutaneous Hyperaesthesia in SARS-CoV-2 Infection: Rare but not Unique Clinical Manifestation. Acta Derm Venereol *101*, adv00366.

Lamb, J., Crawford, E.D., Peck, D., Modell, J.W., Blat, I.C., Wrobel, M.J., Lerner, J., Brunet, J.P., Subramanian, A., Ross, K.N., *et al.* (2006). The Connectivity Map: using gene-expression signatures to connect small molecules, genes, and disease. Science *313*, 1929-1935.

Lawrie, C.H., Gal, S., Dunlop, H.M., Pushkaran, B., Liggins, A.P., Pulford, K., Banham, A.H., Pezzella, F., Boultwood, J., Wainscoat, J.S., *et al.* (2008). Detection of elevated levels of tumour-associated microRNAs in serum of patients with diffuse large B-cell lymphoma. Br J Haematol *141*, 672-675.

Ledford, H. (2020). Coronavirus breakthrough: dexamethasone is first drug shown to save lives. Nature *582*, 469.

Li, J., Li, T., Lu, Y., Shen, G., Guo, H., Wu, J., Lei, C., Du, F., Zhou, F., Zhao, X., *et al.* (2017). MiR-2392 suppresses metastasis and epithelial-mesenchymal transition by targeting MAML3 and WHSC1 in gastric cancer. FASEB J *31*, 3774-3786.

Li, K., Chen, G., Hou, H., Liao, Q., Chen, J., Bai, H., Lee, S., Wang, C., Li, H., Cheng, L., *et al.* (2021). Analysis of sex hormones and menstruation in COVID-19 women of child-bearing age. Reprod Biomed Online *42*, 260-267.

Liu, X., Wang, S., Meng, F., Wang, J., Zhang, Y., Dai, E., Yu, X., Li, X., and Jiang, W. (2013). SM2miR: a database of the experimentally validated small molecules' effects on microRNA expression. Bioinformatics *29*, 409-411.

Lott, M.T., Leipzig, J.N., Derbeneva, O., Xie, H.M., Chalkia, D., Sarmady, M., Procaccio, V., and Wallace, D.C. (2013). mtDNA Variation and Analysis Using Mitomap and Mitomaster. Curr Protoc Bioinformatics *44*, 1 23 21-26.

Love, M.I., Huber, W., and Anders, S. (2014). Moderated estimation of fold change and dispersion for RNA-seq data with DESeq2. Genome Biol *15*, 550.

Loza, M.J., McCall, C.E., Li, L., Isaacs, W.B., Xu, J., and Chang, B.L. (2007). Assembly of inflammation-related genes for pathway-focused genetic analysis. PLoS One *2*, e1035.

Lui, W.O., Pourmand, N., Patterson, B.K., and Fire, A. (2007). Patterns of known and novel small RNAs in human cervical cancer. Cancer Res *67*, 6031-6043.

Ma, Y., Wang, C., Xue, M., Fu, F., Zhang, X., Li, L., Yin, L., Xu, W., Feng, L., and Liu, P. (2018). The Coronavirus Transmissible Gastroenteritis Virus Evades the Type I Interferon Response through IRE1alpha-Mediated Manipulation of the MicroRNA miR-30a-5p/SOCS1/3 Axis. J Virol *92*.

Mahajan, A., and Mason, G.F. (2021). A sobering addition to the literature on COVID-19 and the brain. J Clin Invest.

Malik, Z.R., Razaq, Z., Siff, M., and Sheikh, S. (2020). COVID-19 Presenting as Banti's Syndrome. Cureus *12*, e9096.

Mishra, P.K., Tandon, R., and Byrareddy, S.N. (2020). Diabetes and COVID-19 risk: an miRNA perspective. Am J Physiol Heart Circ Physiol *319*, H604-H609.

Mitchell, P.S., Parkin, R.K., Kroh, E.M., Fritz, B.R., Wyman, S.K., Pogosova-Agadjanyan, E.L., Peterson, A., Noteboom, J., O'Briant, K.C., Allen, A., *et al.* (2008). Circulating microRNAs as stable blood-based markers for cancer detection. Proc Natl Acad Sci U S A *105*, 10513-10518.

Nersisyan, S., Engibaryan, N., Gorbonos, A., Kirdey, K., Makhonin, A., and Tonevitsky, A. (2020). Potential role of cellular miRNAs in coronavirus-host interplay. PeerJ *8*, e9994.

Nishiga, M., Wang, D.W., Han, Y., Lewis, D.B., and Wu, J.C. (2020). COVID-19 and cardiovascular disease: from basic mechanisms to clinical perspectives. Nat Rev Cardiol *17*, 543-558.

Ochsner, S.A., Pillich, R.T., and McKenna, N.J. (2020). Consensus transcriptional regulatory networks of coronavirus-infected human cells. Sci Data *7*, 314.

Ottosen, S., Parsley, T.B., Yang, L., Zeh, K., van Doorn, L.J., van der Veer, E., Raney, A.K., Hodges, M.R., and Patick, A.K. (2015). In vitro antiviral activity and preclinical and clinical resistance profile of miravirsen, a novel anti-hepatitis C virus therapeutic targeting the human factor miR-122. Antimicrob Agents Chemother *59*, 599-608.

Overbey, E.G., Saravia-Butler, A.M., Zhang, Z., Rathi, K.S., Fogle, H., da Silveira, W.A., Barker, R.J., Bass, J.J., Beheshti, A., Berrios, D.C., *et al.* (2021). NASA GeneLab RNA-seq consensus pipeline: standardized processing of short-read RNA-seq data. iScience *24*.

Park, J., Foox, J., Hether, T., Danko, D., Warren, S., Kim, Y., Reeves, J., Butler, D.J., Mozsary, C., Rosiene, J., *et al.* (2021). Systemic Tissue and Cellular Disruption from SARS-CoV-2 Infection revealed in COVID-19 Autopsies and Spatial Omics Tissue Maps. bioRxiv, 2021.2003.2008.434433.

Patro, R., Duggal, G., Love, M.I., Irizarry, R.A., and Kingsford, C. (2017). Salmon provides fast and bias-aware quantification of transcript expression. Nat Methods *14*, 417-419.

Polack, F.P., Thomas, S.J., Kitchin, N., Absalon, J., Gurtman, A., Lockhart, S., Perez, J.L., Perez Marc, G., Moreira, E.D., Zerbini, C., *et al.* (2020). Safety and Efficacy of the BNT162b2 mRNA Covid-19 Vaccine. N Engl J Med *383*, 2603-2615.

Poppe, M., Wittig, S., Jurida, L., Bartkuhn, M., Wilhelm, J., Muller, H., Beuerlein, K., Karl, N., Bhuju, S., Ziebuhr, J., *et al.* (2017). The NF-kappaB-dependent and -independent transcriptome and chromatin landscapes of human coronavirus 229E-infected cells. PLoS Pathog *13*, e1006286.

Portincasa, P., Krawczyk, M., Machill, A., Lammert, F., and Di Ciaula, A. (2020). Hepatic consequences of COVID-19 infection. Lapping or biting? Eur J Intern Med *77*, 18-24.

Rath, S., Sharma, R., Gupta, R., Ast, T., Chan, C., Durham, T.J., Goodman, R.P., Grabarek, Z., Haas, M.E., Hung, W.H.W., *et al.* (2021). MitoCarta3.0: an updated mitochondrial proteome now with sub-organelle localization and pathway annotations. Nucleic Acids Res *49*, D1541-D1547.

Ren, L., Zhang, R., Rao, J., Xiao, Y., Zhang, Z., Yang, B., Cao, D., Zhong, H., Ning, P., Shang, Y., *et al.* (2018). Transcriptionally Active Lung Microbiome and Its Association with Bacterial Biomass and Host Inflammatory Status. mSystems *3*.

Ritchie, M.E., Phipson, B., Wu, D., Hu, Y., Law, C.W., Shi, W., and Smyth, G.K. (2015). limma powers differential expression analyses for RNA-sequencing and microarray studies. Nucleic Acids Res *43*, e47.

Rodriguez, M., Soler, Y., Perry, M., Reynolds, J.L., and El-Hage, N. (2020). Impact of Severe Acute Respiratory Syndrome Coronavirus 2 (SARS-CoV-2) in the Nervous System: Implications of COVID-19 in Neurodegeneration. Front Neurol *11*, 583459.

Rossi, R., Talarico, M., Coppi, F., and Boriani, G. (2020). Protective role of statins in COVID 19 patients: importance of pharmacokinetic characteristics rather than intensity of action. Intern Emerg Med *15*, 1573-1576.

Rother, N., Yanginlar, C., Lindeboom, R.G.H., Bekkering, S., van Leent, M.M.T., Buijsers, B., Jonkman, I., de Graaf, M., Baltissen, M., Lamers, L.A., *et al.* (2020). Hydroxychloroquine Inhibits the Trained Innate Immune Response to Interferons. Cell Rep Med *1*, 100146.

Rupaimoole, R., and Slack, F.J. (2017). MicroRNA therapeutics: towards a new era for the management of cancer and other diseases. Nat Rev Drug Discov *16*, 203-222.

Sacar Demirci, M.D., and Adan, A. (2020). Computational analysis of microRNA-mediated interactions in SARS-CoV-2 infection. PeerJ *8*, e9369.

Sadoff, J., Le Gars, M., Shukarev, G., Heerwegh, D., Truyers, C., de Groot, A.M., Stoop, J., Tete, S., Van Damme, W., Leroux-Roels, I., *et al.* (2021). Interim Results of a Phase 1-2a Trial of Ad26.COV2.S Covid-19 Vaccine. N Engl J Med.

Sardar, R., Satish, D., and Gupta, D. (2020). Identification of Novel SARS-CoV-2 Drug Targets by Host MicroRNAs and Transcription Factors Co-regulatory Interaction Network Analysis. Front Genet *11*, 571274.

Schult, P., Roth, H., Adams, R.L., Mas, C., Imbert, L., Orlik, C., Ruggieri, A., Pyle, A.M., and Lohmann, V. (2018). microRNA-122 amplifies hepatitis C virus translation by shaping the structure of the internal ribosomal entry site. Nat Commun *9*, 2613.

Self, W.H., Tenforde, M.W., Stubblefield, W.B., Feldstein, L.R., Steingrub, J.S., Shapiro, N.I., Ginde, A.A., Prekker, M.E., Brown, S.M., Peltan, I.D., *et al.* (2020). Decline in SARS-CoV-2 Antibodies After Mild Infection Among Frontline Health Care Personnel in a Multistate Hospital Network - 12 States, April-August 2020. MMWR Morb Mortal Wkly Rep *69*, 1762-1766.

Shannon, P., Markiel, A., Ozier, O., Baliga, N.S., Wang, J.T., Ramage, D., Amin, N., Schwikowski, B., and Ideker, T. (2003). Cytoscape: a software environment for integrated models of biomolecular interaction networks. Genome Res *13*, 2498-2504.

Shen, Z., Xiao, Y., Kang, L., Ma, W., Shi, L., Zhang, L., Zhou, Z., Yang, J., Zhong, J., Yang, D., *et al.* (2020). Genomic Diversity of Severe Acute Respiratory Syndrome-Coronavirus 2 in Patients With Coronavirus Disease 2019. Clin Infect Dis *71*, 713-720.

Shu, Y., and McCauley, J. (2017). GISAID: Global initiative on sharing all influenza data - from vision to reality. Euro Surveill *22*.

Singh, U., Hur, M., Dorman, K., and Wurtele, E.S. (2020). MetaOmGraph: a workbench for interactive exploratory data analysis of large expression datasets. Nucleic Acids Res *48*, e23.

Sirin, D.A., and Ozcelik, F. (2021). The relationship between COVID-19 and the dental damage stage determined by radiological examination. Oral Radiol.

Sirota, M., Dudley, J.T., Kim, J., Chiang, A.P., Morgan, A.A., Sweet-Cordero, A., Sage, J., and Butte, A.J. (2011). Discovery and preclinical validation of drug indications using compendia of public gene expression data. Sci Transl Med *3*, 96ra77.

Souza, W.M., Amorim, M.R., Sesti-Costa, R., Coimbra, L.D., Brunetti, N.S., Toledo-Teixeira, D.A., de Souza, G.F., Muraro, S.P., Parise, P.L., Barbosa, P.P., *et al.* (2021). Neutralisation of SARS-CoV-2 lineage P.1 by antibodies elicited through natural SARS-CoV-2 infection or vaccination with an inactivated SARS-CoV-2 vaccine: an immunological study. Lancet Microbe.

Stukalov, A., Girault, V., Grass, V., Karayel, O., Bergant, V., Urban, C., Haas, D.A., Huang, Y., Oubraham, L., Wang, A., *et al.* (2021). Multilevel proteomics reveals host perturbations by SARS-CoV-2 and SARS-CoV. bioRxiv, 2020.2006.2017.156455.

Su, M., Chen, Y., Qi, S., Shi, D., Feng, L., and Sun, D. (2020). A Mini-Review on Cell Cycle Regulation of Coronavirus Infection. Front Vet Sci *7*, 586826.

Subramanian, A., Tamayo, P., Mootha, V.K., Mukherjee, S., Ebert, B.L., Gillette, M.A., Paulovich, A., Pomeroy, S.L., Golub, T.R., Lander, E.S., *et al.* (2005). Gene set enrichment analysis: a knowledge-based approach for interpreting genome-wide expression profiles. Proc Natl Acad Sci U S A *102*, 15545-15550.

Sullivan, K.D., Galbraith, M.D., Kinning, K.T., Bartsch, K., Levinsky, N., Araya, P., Smith, K.P., Granrath, R.E., Shaw, J.R., Baxter, R., *et al.* (2021). The COVIDome Explorer Researcher Portal. medRxiv.

Tang, H., Gao, Y., Li, Z., Miao, Y., Huang, Z., Liu, X., Xie, L., Li, H., Wen, W., Zheng, Y., *et al.* (2020). The noncoding and coding transcriptional landscape of the peripheral immune response in patients with COVID-19. Clin Transl Med *10*, e200.

Teodori, L., Sestili, P., Madiai, V., Coppari, S., Fraternale, D., Rocchi, M.B.L., Ramakrishna, S., and Albertini, M.C. (2020). MicroRNAs Bioinformatics Analyses Identifying HDAC Pathway as a Putative Target for Existing Anti-COVID-19 Therapeutics. Front Pharmacol *11*, 582003.

Thibault, P.A., Huys, A., Amador-Canizares, Y., Gailius, J.E., Pinel, D.E., and Wilson, J.A. (2015). Regulation of Hepatitis C Virus Genome Replication by Xrn1 and MicroRNA-122 Binding to Individual Sites in the 5' Untranslated Region. J Virol *89*, 6294-6311.

Toniolo, P.A., Liu, S., Yeh, J.E., Moraes-Vieira, P.M., Walker, S.R., Vafaizadeh, V., Barbuto, J.A., and Frank, D.A. (2015). Inhibiting STAT5 by the BET bromodomain inhibitor JQ1 disrupts human dendritic cell maturation. J Immunol *194*, 3180-3190.

Tribolet, L., Kerr, E., Cowled, C., Bean, A.G.D., Stewart, C.R., Dearnley, M., and Farr, R.J. (2020). MicroRNA Biomarkers for Infectious Diseases: From Basic Research to Biosensing. Front Microbiol *11*, 1197.

Trobaugh, D.W., and Klimstra, W.B. (2017). MicroRNA Regulation of RNA Virus Replication and Pathogenesis. Trends Mol Med *23*, 80-93.

V'Kovski, P., Kratzel, A., Steiner, S., Stalder, H., and Thiel, V. (2021). Coronavirus biology and replication: implications for SARS-CoV-2. Nat Rev Microbiol *19*, 155-170.

van der Ree, M.H., de Vree, J.M., Stelma, F., Willemse, S., van der Valk, M., Rietdijk, S., Molenkamp, R., Schinkel, J., van Nuenen, A.C., Beuers, U., *et al.* (2017). Safety, tolerability, and antiviral effect of RG-101 in patients with chronic hepatitis C: a phase 1B, double-blind, randomised controlled trial. Lancet *389*, 709-717.

Vejnar, C.E., and Zdobnov, E.M. (2012). MiRmap: comprehensive prediction of microRNA target repression strength. Nucleic Acids Res *40*, 11673-11683.

Wallace, D.C. (2018). Mitochondrial genetic medicine. Nat Genet *50*, 1642-1649.

West, A.P., and Shadel, G.S. (2017). Mitochondrial DNA in innate immune responses and inflammatory pathology. Nat Rev Immunol *17*, 363-375.

Wickham, H. (2016). ggplot2: Elegant Graphics for Data Analysis (Springer-Verlag New York).

Yang, J., Li, C., Li, H., and E, C. (2019). LncRNA CACNA1G-AS1 facilitates hepatocellular carcinoma progression through the miR-2392/C1orf61 pathway. J Cell Physiol *234*, 18415-18422.

Yang, S., Pei, Y., Li, X., Zhao, S., Zhu, M., and Zhao, A. (2016). miR-124 attenuates Japanese encephalitis virus replication by targeting DNM2. Virol J *13*, 105.

Younis, J.S., Abassi, Z., and Skorecki, K. (2020). Is there an impact of the COVID-19 pandemic on male fertility? The ACE2 connection. Am J Physiol Endocrinol Metab *318*, E878-E880.

Zamani, B., Moeini Taba, S.M., and Shayestehpour, M. (2021). Systemic lupus erythematosus manifestation following COVID-19: a case report. J Med Case Rep *15*, 29.

Zhong, Z., Liang, S., Sanchez-Lopez, E., He, F., Shalapour, S., Lin, X.J., Wong, J., Ding, S., Seki, E., Schnabl, B., *et al.* (2018). New mitochondrial DNA synthesis enables NLRP3 inflammasome activation. Nature *560*, 198-203.

Zhu, N., Zhang, D., Wang, W., Li, X., Yang, B., Song, J., Zhao, X., Huang, B., Shi, W., Lu, R., *et al.* (2020). A Novel Coronavirus from Patients with Pneumonia in China, 2019. N Engl J Med *382*, 727-733.

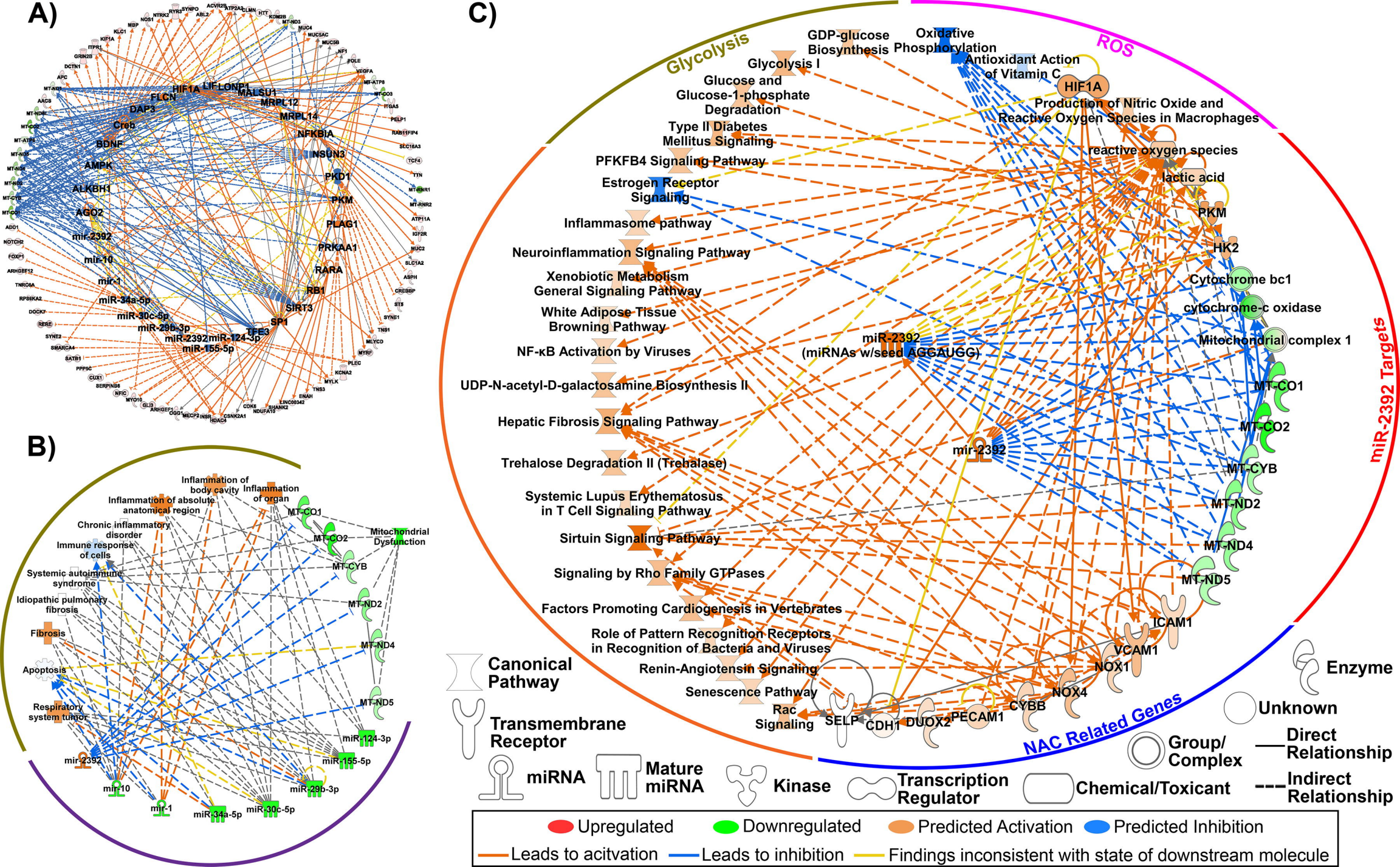
A)
HIF1A
LIF
LONP1
MALSU1
MRPL12
FLCN
DAP3
MRPL14
Creb
NFKBIA
BDNF
NSUN3
AMPK
PKD1
ALKBH1
PKM
AGO2
PLAG1
miR-2392
PRKAA1
miR-10
RARA
miR-1
RB1
miR-34a-5p
SIRT3
miR-30c-5p
miR-29b-3p
SP1
TFE3
miR-2392
miR-124-3p
miR-155-5p
B)
Inflammation of body cavity
Inflammation of organ
Inflammation of absolute anatomical region
MT-CO1
Chronic inflammatory disorder
MT-CO2
Mitochondrial Dysfunction
Immune response of cells
MT-CYB
Systemic autoimmune syndrome
Idiopathic pulmonary fibrosis
MT-ND2
Fibrosis
MT-ND4
Apoptosis
MT-ND5
Respiratory system tumor
miR-124-3p
miR-2392
miR-155-5p
miR-29b-3p
miR-10
miR-1
miR-34a-5p
miR-30c-5p
C)
Glycolysis
ROS
GDP-glucose Biosynthesis
Oxidative Phosphorylation
Glycolysis I
Antioxidant Action of Vitamin C
HIF1A
Glucose and Glucose-1-phosphate Degradation
Production of Nitric Oxide and Reactive Oxygen Species in Macrophages
Type II Diabetes Mellitus Signaling
reactive oxygen species
PFKFB4 Signaling Pathway
lactic acid
Estrogen Receptor Signaling
PKM
Inflammasome pathway
HK2
Neuroinflammation Signaling Pathway
Xenobiotic Metabolism General Signaling Pathway
Cytochrome bc1
cytochrome-c oxidase
White Adipose Tissue Browning Pathway
miR-2392 (miRNAs w/seed AGCAUGG)
Mitochondrial complex 1
NF-κB Activation by Viruses
MT-CO1
UDP-N-acetyl-D-galactosamine Biosynthesis II
MT-CO2
Hepatic Fibrosis Signaling Pathway
mir-2392
Trehalose Degradation II (Trehalase)
MT-CYB
Systemic Lupus Erythematosus in T Cell Signaling Pathway
MT-ND2
Sirtuin Signaling Pathway
MT-ND4
Signaling by Rho Family GTPases
MT-ND5
Factors Promoting Cardiogenesis in Vertebrates
ICAM1
Role of Pattern Recognition Receptors in Recognition of Bacteria and Viruses
VCAM1
Renin-Angiotensin Signaling
NOX1
Senescence Pathway
NOX4
Rac Signaling
SELP
CDH1
DUOX2
PECAM1
CYBB
miR-2392 Targets
NAC Related Genes
Canonical Pathway
Transmembrane Receptor
miRNA
Mature miRNA
Kinase
Transcription Regulator
Chemical/Toxicant
Enzyme
Unknown
Group/ Complex
Direct Relationship
Indirect Relationship
Upregulated
Downregulated
Predicted Activation
Predicted Inhibition
Leads to acitvation
Leads to inhibition
Findings inconsistent with state of downstream molecule

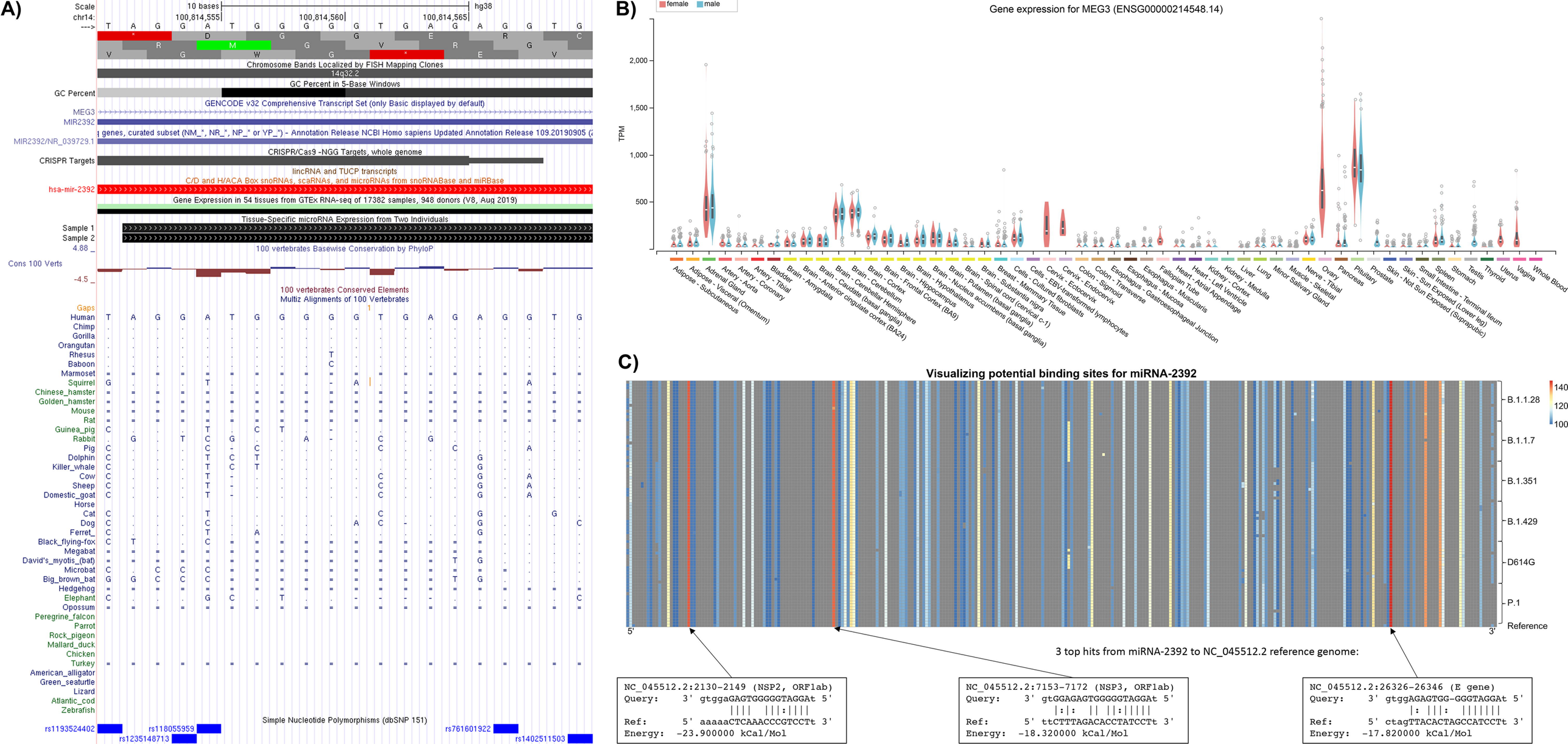
A)
Scale
chr14:
10 bases
hg38
100,814,555
100,814,560
100,814,565
Chromosome Bands Localized by FISH Mapping Clones
14q32.2
GC Percent in 5-Base Windows
GC Percent
GENCODE v32 Comprehensive Transcript Set (only Basic displayed by default)
MEG3
MIR2392
MIR2392/NR_039729.1
CRISPR/Cas9 -NGG Targets, whole genome
CRISPR Targets
lincRNA and TUCP transcripts
C/D and H/ACA Box snoRNAs, scaRNAs, and microRNAs from snoRNABase and miRBase
hsa-mir-2392
Gene Expression in 54 tissues from GTEx RNA-seq of 17382 samples, 948 donors (V8, Aug 2019)
Tissue-Specific microRNA Expression from Two Individuals
Sample 1
Sample 2
100 vertebrates Basewise Conservation by PhyloP
Cons 100 Verts
100 vertebrates Conserved Elements
Multiz Alignments of 100 Vertebrates
Gaps
Human
Chimp
Gorilla
Orangutan
Rhesus
Baboon
Marmoset
Squirrel
Chinese_hamster
Golden_hamster
Mouse
Rat
Guinea_pig
Rabbit
Pig
Dolphin
Killer_whale
Cow
Sheep
Domestic_goat
Horse
Cat
Dog
Ferret
Black_flying-fox
Megabat
David's_myotis_(bat)
Microbat
Big_brown_bat
Hedgehog
Elephant
Opossum
Peregrine_falcon
Parrot
Rock_pigeon
Mallard_duck
Chicken
Turkey
American_alligator
Green_seaturtle
Lizard
Atlantic_cod
Zebrafish
Simple Nucleotide Polymorphisms (dbSNP 151)
rs1193524402
rs118055959
rs1235148713
rs761601922
rs1402511503
B)
female
male
Gene expression for MEG3 (ENSG00000214548.14)
TPM
2,000
1,500
1,000
500
Adipose - Subcutaneous
Adipose - Visceral (Omentum)
Adrenal Gland
Artery - Aorta
Artery - Coronary
Artery - Tibial
Bladder
Brain - Amygdala
Brain - Anterior cingulate cortex (BA24)
Brain - Caudate (basal ganglia)
Brain - Cerebellar Hemisphere
Brain - Cerebellum
Brain - Cortex
Brain - Frontal Cortex (BA9)
Brain - Hippocampus
Brain - Hypothalamus
Brain - Nucleus accumbens (basal ganglia)
Brain - Putamen (basal ganglia)
Brain - Spinal cord (cervical c-1)
Brain - Substantia nigra
Breast - Mammary Tissue
Cells - Cultured fibroblasts
Cells - EBV-transformed lymphocytes
Cervix - Ectocervix
Cervix - Endocervix
Colon - Sigmoid
Colon - Transverse
Esophagus - Gastroesophageal Junction
Esophagus - Mucosa
Esophagus - Muscularis
Fallopian Tube
Heart - Atrial Appendage
Heart - Left Ventricle
Kidney - Cortex
Kidney - Medulla
Liver
Lung
Minor Salivary Gland
Muscle - Skeletal
Nerve - Tibial
Ovary
Pancreas
Pituitary
Prostate
Skin - Not Sun Exposed (Suprapubic)
Skin - Sun Exposed (Lower leg)
Small Intestine - Terminal Ileum
Spleen
Stomach
Testis
Thyroid
Uterus
Vagina
Whole Blood
C)
Visualizing potential binding sites for miRNA-2392
140
120
100
B.1.1.28
B.1.1.7
B.1.351
B.1.429
D614G
P.1
Reference
5'
3'
3 top hits from miRNA-2392 to NC_045512.2 reference genome:
NC_045512.2:2130-2149 (NSP2, ORF1ab)
Query: 3' gtggaGAGTGGGGGTAGGAt 5'
|||| |||:||||
Ref: 5' aaaaaCTCAAACCCGTCCTt 3'
Energy: -23.900000 kCal/Mol
NC_045512.2:7153-7172 (NSP3, ORF1ab)
Query: 3' gtGGAGAGTGGGGGTAGGAt 5'
|:|: || ||:|||||
Ref: 5' ttCTTTAGACACCTATCCTt 3'
Energy: -18.320000 kCal/Mol
NC_045512.2:26326-26346 (E gene)
Query: 3' gtggAGAGTGG-GGGTAGGAt 5'
|: |||: |||||||
Ref: 5' ctagTTACACTAGCCATCCTt 3'
Energy: -17.820000 kCal/Mol

miR-2392 Targets in COVID-19 Patients

Not sig. · Log_2 fold change · FDR · FDR & Log_2 fold change

A) Nasal Swab: High vs Neg · Nasal Swab: Medium vs Neg · Nasal Swab: Low vs Neg

B) Heart: High vs Neg · Heart: Low vs Neg

C) Kidney: High vs Neg · Kidney: Low vs Neg

D) Liver: High vs Neg · Liver: Low vs Neg

E) Lung: High vs Neg · Lung: Low vs Neg

F) Lymph Node: High vs Neg · Lymph Node: Low vs Neg

$-Log_{10}$ FDR · Log_2 fold change

G) miR−2392 Targets

Regulation of sprouting angiogenesis
Regulation of axonogenesis
Nervous system development
Calcium ion binding
Exopeptidase activity
Developmental Biology
Semaphorin interactions
Metabolism of polyamines
Transport of small molecules
G0 and Early G1
Apoptosis
Mitotic G1−G1/S phases
Oligopeptide transmembrane transporter activity
Oxidoreductase activity
Enzyme binding
Protein kinase A catalytic subunit binding
Ubiquitin binding
Response to organic substance
Insulin receptor signaling pathway
Hemostasis
TRAIL signaling
Signaling by FGFR and EGFR in disease
IGF1R signaling cascade
P53 Pathway
TNFA Signaling via NFKB
Synaptic vesicle transport
Regulation of biological quality
Response to ether
Adhesion of symbiont to host cell
Pigment accumulation
Response to vitamin E
Paranodal junction assembly
Transcriptional Regulation by TP53
G alpha (i) signalling events
Immune System
Interferon Signaling
Defense response to virus
Cluster
Down Reg
Up Reg
Common Sig
miRmap score
deltaG open
Tissue
Viral Load

H) Mitochondrial miR−2392 Targets

SLC25A28, MSRB3, NDUFS5, TOMM20, MTHFD2L, AK4, COX10, MRS2, MRPL34, COX6B1, GOT2, CLIC4, CKMT1A, IBA57

Viral Load: High vs Neg, Medium vs Neg, Low vs Neg
Tissue: Nasal, Heart, Kidney, Liver, Lung, Lymph Node
Down Reg: 13 / 0
Up Reg: 13 / 0
t scores: 10, 5, 0, −5
Common Sig: 7 / 1
miRmap score: 80 / 20
deltaG open: 80 / 20

I) Inflammation miR−2392 Targets

IFNAR2, KLRK1, UBE2N, PIK3CA, YWHAZ, NRAS, CARD8, PSMB5, PRKAR2A, PPM1A, TNFRSF10D, PIAS2, CAMK1D, PPP3CA, TNFRSF10B, ACIN1, CD209, SELL, CCND1, SIGLEC1, CXCL9, CASP10

Primary Pathway: Adhesion−Extravasation−Migration, Apoptosis Signaling, Calcium Signaling, Cytokine signaling, G−Protein Coupled Receptor Signaling, Innate pathogen detection, MAPK signaling, Natural Killer Cell Signaling, NF−kB signaling, Phagocytosis−Ag presentation, PI3K/AKT Signaling

J) Fold change difference between transcriptome and proteome for miR-2392 targets
p-value <= 0.05 for RNA transcripts

Protein log2 Fold Change · RNA transcript log2 Fold Change
Cutoff guidelines: 1 log2 Fold Change, 2 log2 Fold Change · Significance: Lower, Higher

K) RNA-Protein correlation for miR-2392 targets
Pearson correlation for COVID-19 positive: 0.205
Pearson correlation for COVID-19 negative: 0.209
Protein log2 adjusted relative abundance · RNA log2 RPKM
COVID-19 status: Negative, Positive · RNA transcript log2 Fold Change · Fold Change direction: Positive, Negative

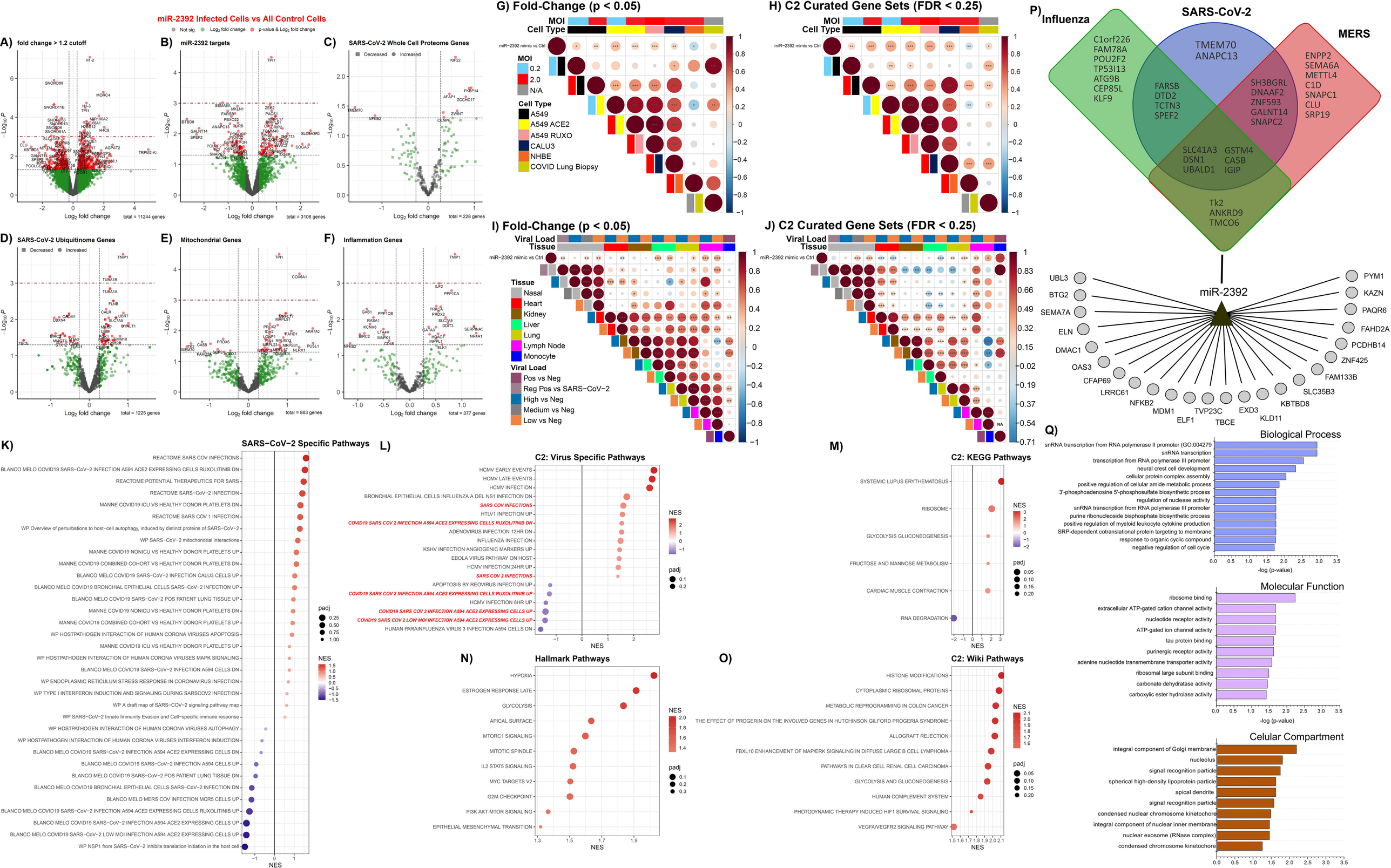
miR-2392 Infected Cells vs All Control Cells
Not sig.
Log2 fold change
p-value & Log2 fold change
A) fold change > 1.2 cutoff
B) miR-2392 targets
C) SARS-CoV-2 Whole Cell Proteome Genes
Decreased
Increased
D) SARS-CoV-2 Ubiquitinome Genes
E) Mitochondrial Genes
F) Inflammation Genes
Log2 fold change
total = 11244 genes
total = 3108 genes
total = 228 genes
total = 1225 genes
total = 883 genes
total = 377 genes
G) Fold-Change (p < 0.05)
H) C2 Curated Gene Sets (FDR < 0.25)
MOI
Cell Type
miR−2392 mimic vs Ctrl
0.2
2.0
N/A
A549
A549 ACE2
A549 RUXO
CALU3
NHBE
COVID Lung Biopsy
I) Fold-Change (p < 0.05)
J) C2 Curated Gene Sets (FDR < 0.25)
Viral Load
Tissue
Nasal
Heart
Kidney
Liver
Lung
Lymph Node
Monocyte
Pos vs Neg
Reg Pos vs SARS−CoV−2
High vs Neg
Medium vs Neg
Low vs Neg
P)
Influenza
SARS-CoV-2
MERS
C1orf226
FAM78A
POU2F2
TP53I13
ATG9B
CEP85L
KLF9
TMEM70
ANAPC13
FARSB
DTD2
TCTN3
SPEF2
SH3BGRL
DNAAF2
ZNF593
GALNT14
SNAPC2
ENPP2
SEMA6A
METTL4
C1D
SNAPC1
CLU
SRP19
SLC41A3
DSN1
UBALD1
GSTM4
CA5B
IGIP
Tk2
ANKRD9
TMCO6
miR-2392
UBL3
BTG2
SEMA7A
ELN
DMAC1
OAS3
CFAP69
LRRC61
NFKB2
MDM1
ELF1
TVP23C
TBCE
EXD3
KLD11
KBTBD8
SLC35B3
FAM133B
ZNF425
PCDHB14
FAHD2A
PAQR6
KAZN
PYM1
K) SARS−CoV−2 Specific Pathways
L) C2: Virus Specific Pathways
M) C2: KEGG Pathways
N) Hallmark Pathways
O) C2: Wiki Pathways
Q) Biological Process
Molecular Function
Celular Compartment
NES
padj

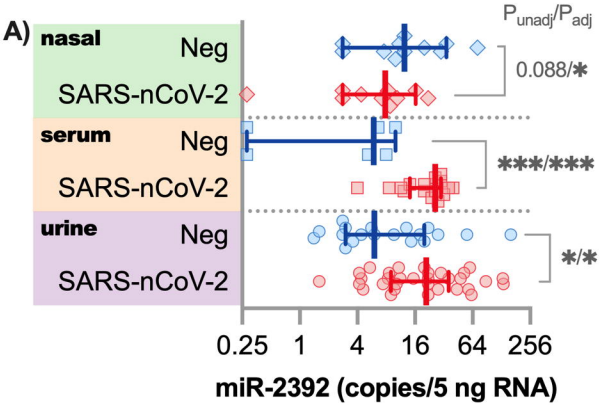

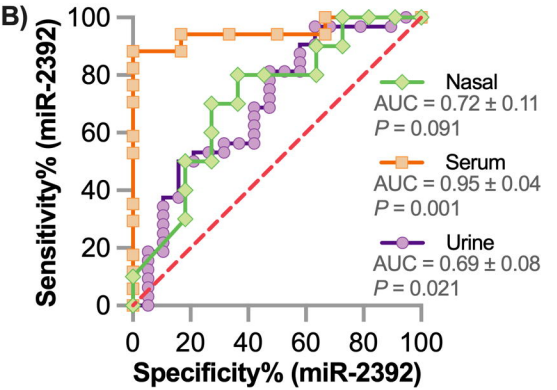

unadjusted = t-test Neg vs SARS-nCoV-2 (on log values)
adjusted = mixed model corrected for age and sex (single terms)
*, **, *** = P < 0.05, 0.01, 0.001

AUC = area under the curve

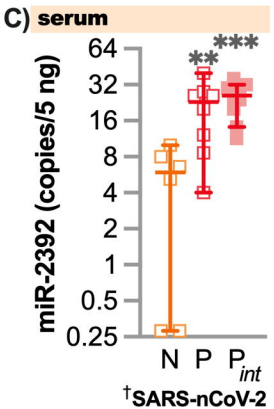

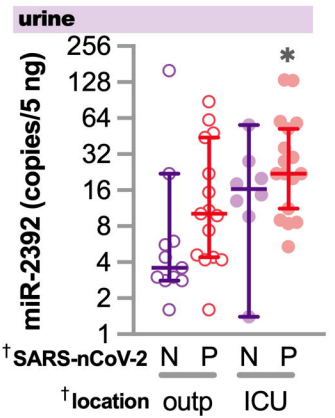

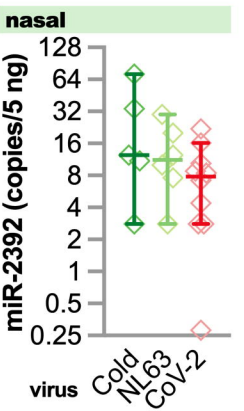

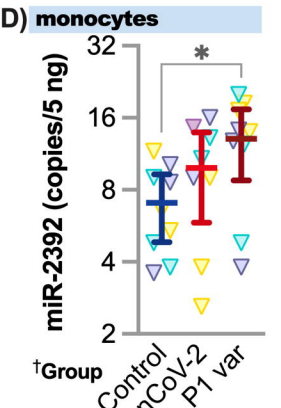

nasal & serum = ANOVA, urine = 2way ANOVA
†, †† = P < 0.05, 0.01 ANOVA on glog values
*, **, *** = P < 0.05, 0.01, 0.001 Dunnet's post-test compared to Neg

† = P < 0.05 ANOVA-RM on glog values
* = P < 0.05 Tukey HSD

monocytes
Donor 1
Donor 2
Donor 3

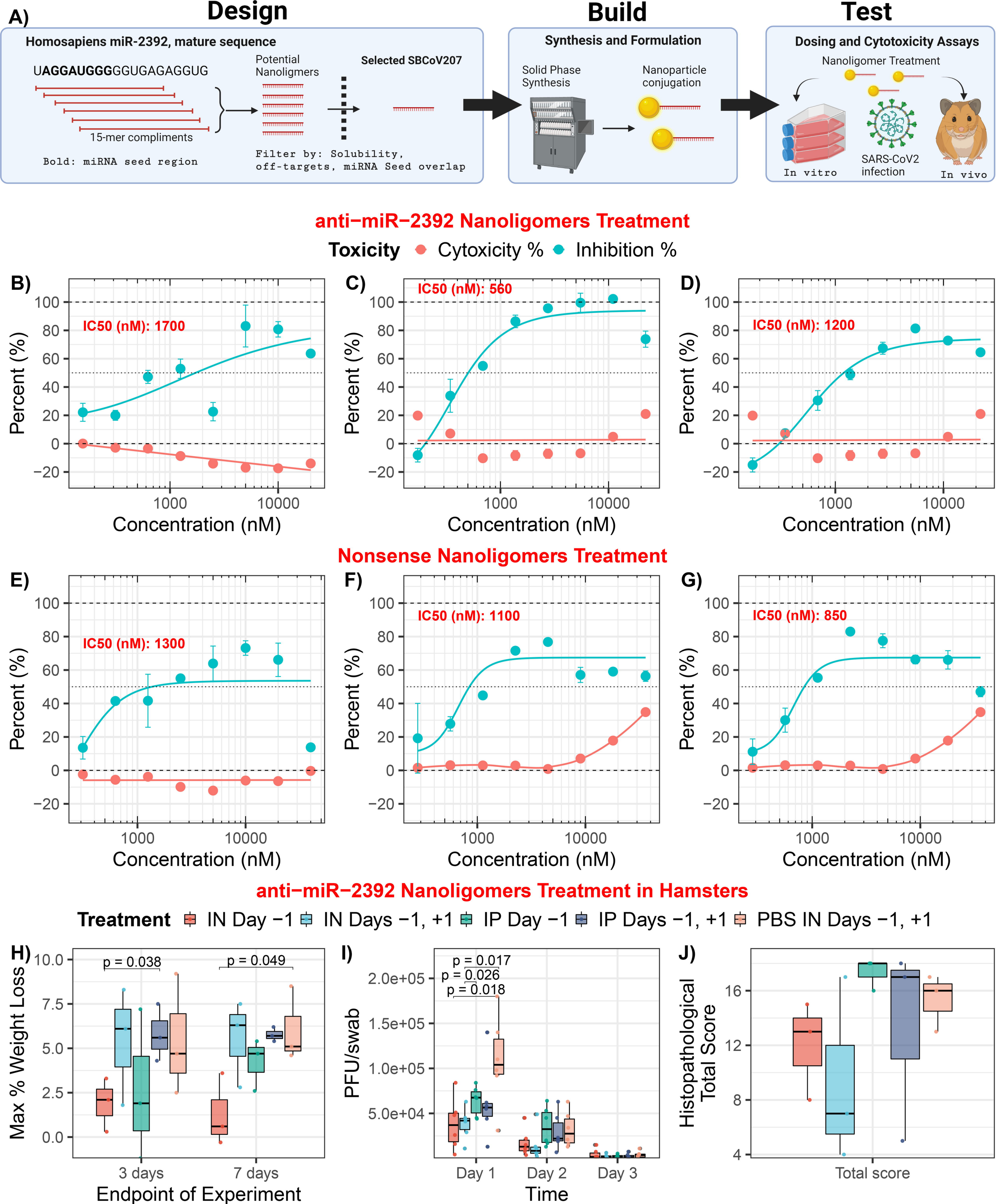
A)
Design
Homosapiens miR-2392, mature sequence
UAGGAUGGGGGUGAGAGGUG
15-mer compliments
Bold: miRNA seed region
Potential Nanoligmers
Selected SBCoV207
Filter by: Solubility, off-targets, miRNA Seed overlap
Build
Synthesis and Formulation
Solid Phase Synthesis
Nanoparticle conjugation
Test
Dosing and Cytotoxicity Assays
Nanoligomer Treatment
In vitro
SARS-CoV2 infection
In vivo
anti−miR−2392 Nanoligomers Treatment
Toxicity
Cytoxicity %
Inhibition %
B)
IC50 (nM): 1700
C)
IC50 (nM): 560
D)
IC50 (nM): 1200
Percent (%)
Concentration (nM)
Nonsense Nanoligomers Treatment
E)
IC50 (nM): 1300
F)
IC50 (nM): 1100
G)
IC50 (nM): 850
anti−miR−2392 Nanoligomers Treatment in Hamsters
Treatment
IN Day −1
IN Days −1, +1
IP Day −1
IP Days −1, +1
PBS IN Days −1, +1
H)
p = 0.038
p = 0.049
Max % Weight Loss
3 days
7 days
Endpoint of Experiment
I)
p = 0.017
p = 0.026
p = 0.018
PFU/swab
Day 1
Day 2
Day 3
Time
J)
Histopathological Total Score
Total score

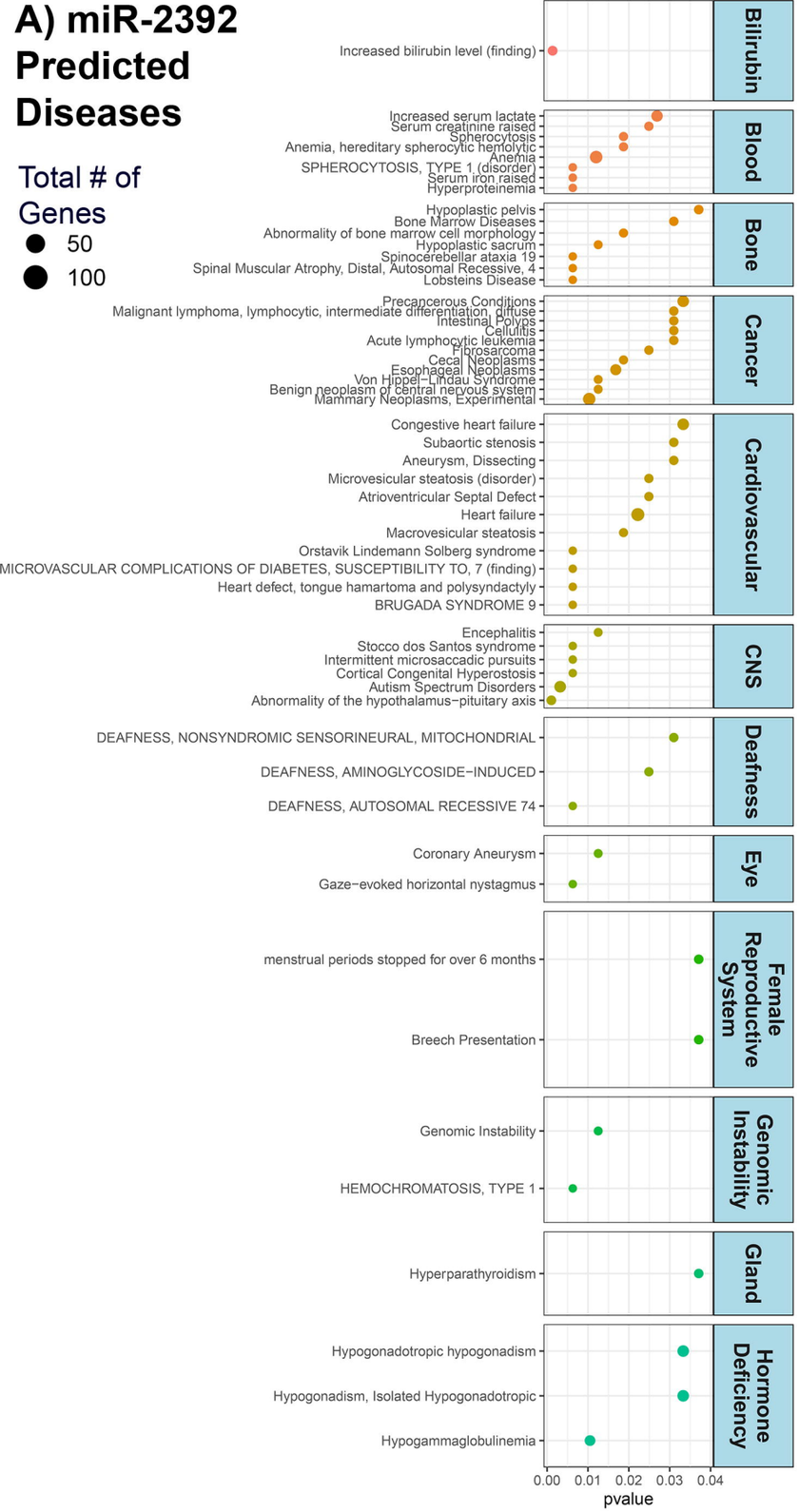
A) miR-2392 Predicted Diseases
Total # of Genes
50
100
Bilirubin
Increased bilirubin level (finding)
Blood
Increased serum lactate
Serum creatinine raised
Spherocytosis
Anemia, hereditary spherocytic hemolytic
Anemia
SPHEROCYTOSIS, TYPE 1 (disorder)
Serum iron raised
Hyperproteinemia
Bone
Hypoplastic pelvis
Bone Marrow Diseases
Abnormality of bone marrow cell morphology
Hypoplastic sacrum
Spinocerebellar ataxia 19
Spinal Muscular Atrophy, Distal, Autosomal Recessive, 4
Lobsteins Disease
Cancer
Precancerous Conditions
Malignant lymphoma, lymphocytic, intermediate differentiation, diffuse
Intestinal Polyps
Cellulitis
Acute lymphocytic leukemia
Fibrosarcoma
Cecal Neoplasms
Esophageal Neoplasms
Von Hippel−Lindau Syndrome
Benign neoplasm of central nervous system
Mammary Neoplasms, Experimental
Cardiovascular
Congestive heart failure
Subaortic stenosis
Aneurysm, Dissecting
Microvesicular steatosis (disorder)
Atrioventricular Septal Defect
Heart failure
Macrovesicular steatosis
Orstavik Lindemann Solberg syndrome
MICROVASCULAR COMPLICATIONS OF DIABETES, SUSCEPTIBILITY TO, 7 (finding)
Heart defect, tongue hamartoma and polysyndactyly
BRUGADA SYNDROME 9
CNS
Encephalitis
Stocco dos Santos syndrome
Intermittent microsaccadic pursuits
Cortical Congenital Hyperostosis
Autism Spectrum Disorders
Abnormality of the hypothalamus−pituitary axis
Deafness
DEAFNESS, NONSYNDROMIC SENSORINEURAL, MITOCHONDRIAL
DEAFNESS, AMINOGLYCOSIDE−INDUCED
DEAFNESS, AUTOSOMAL RECESSIVE 74
Eye
Coronary Aneurysm
Gaze−evoked horizontal nystagmus
Female Reproductive System
menstrual periods stopped for over 6 months
Breech Presentation
Genomic Instability
Genomic Instability
HEMOCHROMATOSIS, TYPE 1
Gland
Hyperparathyroidism
Hormone Deficiency
Hypogonadotropic hypogonadism
Hypogonadism, Isolated Hypogonadotropic
Hypogammaglobulinemia
0.00 0.01 0.02 0.03 0.04
pvalue

Immune
Increased IgM levels
Cholangitis
Hereditary spherocytosis
Reduced natural killer cell activity
X−Linked Lymphoproliferative Disorder
Increased levels of IgG
Decreased antibody level in blood
Hemoglobin low
Lymphoproliferative Syndrome, X−Linked, 2
Abnormal glucose tolerance
Kidney
Kidney Failure, Acute
Liver
Liver enzymes abnormal
Liver function tests abnormal finding
Hepatic enzyme increased
Hepatic Fibrosis, Congenital
Increased hepatocellular lipid droplets
Hepatitis C
Fulminant hepatitis
Hepatomegaly
LIVER FAILURE, INFANTILE, TRANSIENT
Liver Dysfunction
Male Infertility
Azoospermia
Misc
Lead Poisoning
Mitochondrial
Cytochrome−c Oxidase Deficiency
MITOCHONDRIAL MYOPATHY, INFANTILE, TRANSIENT
Pentosuria
Muscle
Hernia, Femoral
Oral
Hamartoma of tongue
Dentinogenesis Imperfecta
CHARCOT−MARIE−TOOTH DISEASE, RECESSIVE INTERMEDIATE C
Respiratory
Pleural effusion disorder
Short Stature
Short femoral neck
Short stature, severe disproportionate
Short stature, disproportionate
SHORT STATURE, ONYCHODYSPLASIA, FACIAL DYSMORPHISM, AND HYPOTRICHOSIS SYNDROME
Skin
Icterus
Porphyria, South African type
Porphyria Cutanea Tarda, Type I
Porphyria Cutanea Tarda
Smell
Hyperesthesia
Sore Throat
Lymphadenopathy
pharyngitis recurrent
Spleen
Splenomegaly
0.00 0.01 0.02 0.03 0.04
pvalue

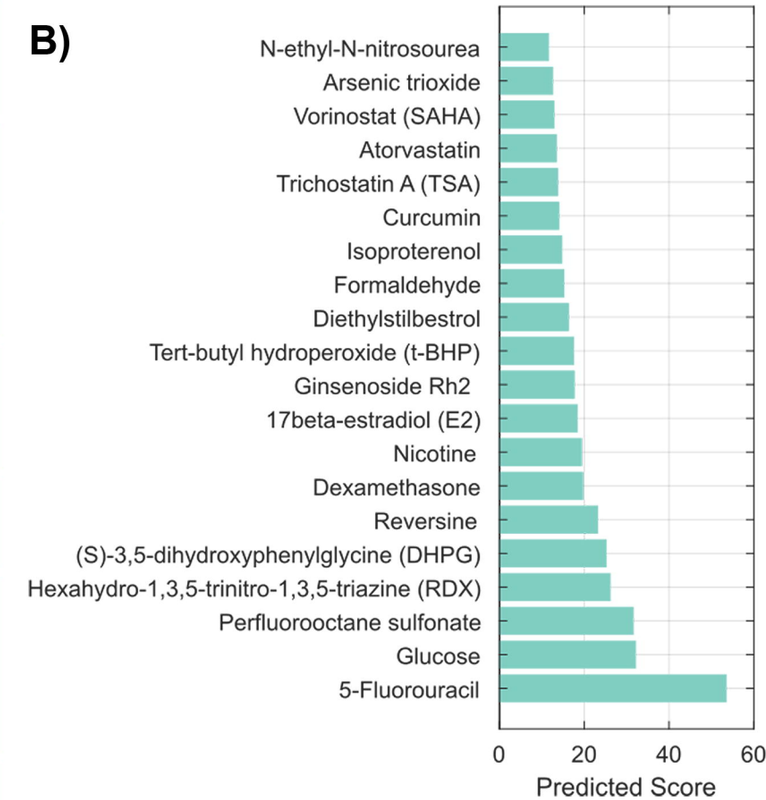
B)
N-ethyl-N-nitrosourea
Arsenic trioxide
Vorinostat (SAHA)
Atorvastatin
Trichostatin A (TSA)
Curcumin
Isoproterenol
Formaldehyde
Diethylstilbestrol
Tert-butyl hydroperoxide (t-BHP)
Ginsenoside Rh2
17beta-estradiol (E2)
Nicotine
Dexamethasone
Reversine
(S)-3,5-dihydroxyphenylglycine (DHPG)
Hexahydro-1,3,5-trinitro-1,3,5-triazine (RDX)
Perfluorooctane sulfonate
Glucose
5-Fluorouracil
0
20
40
60
Predicted Score

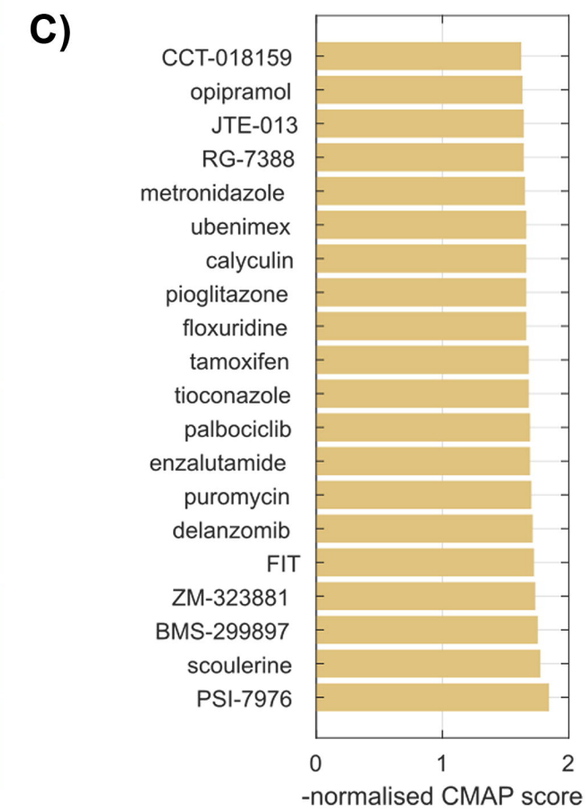
C)
CCT-018159
opipramol
JTE-013
RG-7388
metronidazole
ubenimex
calyculin
pioglitazone
floxuridine
tamoxifen
tioconazole
palbociclib
enzalutamide
puromycin
delanzomib
FIT
ZM-323881
BMS-299897
scoulerine
PSI-7976
0
1
2
-normalised CMAP score